INVESTIGATION OF CRYO-COOLED MICROCOILS FOR MRI

A Thesis

by

RICHARD FRANKLIN GODLEY

Submitted to the Office of Graduate Studies of
Texas A&M University
in partial fulfillment of the requirements for the degree of

MASTER OF SCIENCE

August 2011

Major Subject: Electrical Engineering

INVESTIGATION OF CRYO-COOLED MICROCOILS FOR MRI

A Thesis

by

RICHARD FRANKLIN GODLEY

Submitted to the Office of Graduate Studies of
Texas A&M University
in partial fulfillment of the requirements for the degree of

MASTER OF SCIENCE

Approved by:

Chair of Committee,	Steven M. Wright
Committee Members,	Mary P. McDougall Jim X. Ji Gregory H. Huff
Head of Department,	Costas N. Georghiades

August 2011

Major Subject: Electrical Engineering

ABSTRACT

Investigation of Cryo-Cooled Microcoils for MRI. (August 2011)

Richard Franklin Godley, B.S., LeTourneau University

Chair of Advisory Committee: Dr. Steven M. Wright

When increasing magnetic resonance imaging (MRI) resolution into the micron scale, image signal-to-noise ratio (SNR) can be maintained by using small radiofrequency (RF) coils in close proximity to the sample being imaged. Micro-scale RF coils (microcoils) can be easily fabricated on chip and placed adjacent to a sample under test. However, the high series resistance of microcoils limits the SNR due to the thermal noise generated in the copper. Cryo-cooling is a potential technique to reduce thermal noise in microcoils, thereby recovering SNR.

In this research, copper microcoils of two different geometries have been cryo-cooled using liquid nitrogen. Quality-factor (Q) measurements have been taken to quantify the reduction in resistance due to cryo-cooling. Image SNR has been compared between identical coils at room temperature and liquid nitrogen temperature. The relationship between the drop in series resistance and the increase in image SNR has been analyzed, and these measurements compared to theory.

While cryo-cooling can bring about dramatic increases in SNR, the extremely low temperature of liquid nitrogen is incompatible with living tissue. In general, the useful imaging region of a coil is approximately as deep as the coil diameter, thus cryo-cooling of coils has been limited in the past to larger coils, such that the thickness of a conventional cryostat does not put the sample outside of the optimal imaging region. This research utilizes a scheme of microfluidic cooling (developed in the Texas A&M NanoBio Systems Lab), which greatly reduces the volume of liquid nitrogen required to cryo-cool the coil. Along with a small gas phase nitrogen gap, this eliminates the need for a bulky cryostat.

This thesis includes a review of the existing literature on cryo-cooled coils for MRI, as well as a review of planar pair coils and spiral microcoils in MR applications. Our methods of fabricating and testing these coils are described, and the results explained and analyzed. An image SNR improvement factor of 1.47 was achieved after cryo-cooling of a single planar pair coil, and an improvement factor of 4 was achieved with spiral microcoils.

DEDICATION

To Kaylee

ACKNOWLEDGEMENTS

I would like to thank my advisor, Dr. Wright, for his support and guidance throughout this research. I am grateful to all my committee members, Dr. Wright, Dr. McDougall, Dr. Ji, and Dr. Huff, for investing their time to review this thesis. I would also like to thank Dr. Han, who worked with Dr. Wright to initiate this project.

I have received great support from my lab mates; Dr. Wright's and Dr. McDougall's students helped me come up to speed quickly on MRI techniques, theory, and lab practices. I would especially like to thank Mario Carillo for working with me closely when I first came on to the project. Without Mario's supervision and help early on, this research would have taken much longer. Ke Feng and Jaewon Park also deserve thanks for their work on this project before I came along.

Special thanks are due to Chiwan Koo, in Dr. Han's lab. Chiwan spent countless hours fabricating coils for our experiments. I did not have the resources or the knowledge to fabricate the microcoils or microfluidic structures that are integral to this research.

I would like to thank my parents; they have brought me to this point in life and none of this would be possible without them. Most of all, I want to thank my wife, Kaylee; she has sacrificed so much this year to see me through this time.

NOMENCLATURE

B_0	Static Magnetic Field
ESR	Equivalent Series Resistance
LT	Liquid Nitrogen Temperature
$\overrightarrow{M_0}$	Net Magnetization Vector
MR	Magnetic Resonance
MRI	Magnetic Resonance Imaging
MRSL	Magnetic Resonance Systems Laboratory, College Station, TX
NMR	Nuclear Magnetic Resonance
Q	Quality Factor
RF	Radio Frequency
RT	Room Temperature
SEA	Single Echo Acquisition
SNR	Signal-to-Noise Ratio
T	Temperature (K)

TABLE OF CONTENTS

LIST OF FIGURES

LIST OF TABLES

1. INTRODUCTION: MICROCOILS AND CRYOGENICS IN MRI

1.1 A Short History of MRI

In 1922, Otto Stern and Walther Gerlach showed experimentally that particles have quantized spin states. They devised a clever experiment directing a beam of electrically neutral particles through a magnetic field gradient and observed their deflection due to their magnetic moment.[1] The ability to manipulate the spin states of nuclei - nuclear magnetic resonance (NMR) phenomenon - was first described and measured by Isidor Rabi in 1938,[2] earning him the Nobel Prize in Physics in 1944. Later, in 1946, Felix Bloch and Edward Mills Purcell observed that this could be applied to the resonance of nuclei in solids and liquids when placed inside of a magnetic field. They observed that certain nuclei, such as ^{1}H and ^{31}P, absorbed and then released radio frequency (RF) energy when placed in a magnet of the appropriate strength to cause the spins to resonate at the same frequency as the RF energy.[3] Bloch and Purcell received the Nobel Prize in Physics in 1952. Because the nuclei respond differently, depending on their surrounding molecular structure, the NMR phenomenon permits researchers to conduct NMR spectroscopy, allowing a quick and non-destructive method of determining the chemical make-up of a liquid or solid sample.

NMR spectroscopy was developed further and continues to be used as a valuable chemical analysis tool. It was not until 1973 that Paul Lauterbur reconstructed the first image using NMR. An NMR spectrum measured for spectroscopy gives no positional

---

This thesis follows the style of *Lab on a Chip*.

data; instead it reveals data about the molecular structures surrounding the resonated nuclei in the sample. Lauterbur realized that by placing a sample inside a magnetic field gradient, the spectra would reveal information about the position of nuclei in the sample (because the resonant frequency is proportional to the static magnetic field strength.)[4] Lauterbur was awarded the Nobel Prize in Physiology or Medicine in 2003, sharing it with Peter Mansfield, whose developments made MRI much faster, making medical imaging practical.[5-7]

Since Lauterbur's initial image, MRI has grown into the premier method of medical imaging, and has saved countless lives with its advanced diagnostic capabilities. The details of MRI physics and modern imaging sequences are outside the scope of this thesis; many excellent books are available on these subjects.[8, 9] However, since this research has focused primarily on RF coils for MRI, some background must be given on the design and implementation of RF coils.

1.2 RF Coils

One of the essential components of an NMR system, for imaging or spectroscopy, is the RF coil. When the sample under test is placed inside of a static magnetic field (B_0), the spins of the certain nuclei in the sample begin to precess at a rate called the Larmor frequency. The Larmor relationship states that this frequency is proportional to the strength of the magnetic field. All research in this thesis was performed with a 4.7 T (Tesla) magnet, with a Larmor frequency of 200.128 MHz for ^{1}H. In addition to this precession, a slight majority of the spins will line up with the magnetic field, forming a net magnetization vector, $\overrightarrow{M_0}$. On the macroscopic scale, if RF energy is incident on the nuclei at the Larmor frequency, it will tip this net magnetization. As the spins relax back to the equilibrium state, they will emit RF energy at the Larmor frequency. Thus, an RF coil is necessary for both transmission (excitation) and reception in order to acquire a spectrum or form an image. These transmit and receive operations can be performed by a single RF coil or by separate coils. In fact, arrays of coils can be used for transmit or receive to improve sensitivity and signal-to-noise ratio (SNR), or to improve imaging speed.[10]

1.3 SNR of the MRI Experiment

MRI is considered an SNR-limited technique.[11, 12] The number of spins in a voxel (volume pixel) of sample material is finite. In addition, $\overrightarrow{M_0}$ is very small and is proportional to the static magnetic field strength. Because the signal strength is proportional to $\overrightarrow{M_0}$, high quality imaging requires large superconducting magnets to be used for MRI and NMR spectroscopy. Exciting sufficient signal becomes especially difficult when increasing the resolution of the image. Consider the following example: if resolution is increased isotropically by a factor of 10 (say from 1 mm resolution to 100 µm), the voxel volume (and thereby the MR signal) is decreased by a factor of 1000; therefore, the SNR will decrease by a factor of 1000. Some SNR can be regained by averaging multiple acquisitions, but because SNR only increases as the square root of the number of acquisitions, the above example would require 1 million averages to recover the SNR of the poorer resolution image. This would require tremendously long acquisition times, impractical for live subjects and expensive equipment. Thus, averaging alone is an unacceptable method of recovering SNR. Fortunately, the SNR of MRI can be increased with surface coils and microcoils.

1.4 MRI Surface Coils

By reciprocity, the signal induced in the receive coil from a voxel of tissue will be directly proportional to the magnetic (B) field (perpendicular to the static magnetic field) created at the voxel by unit current in the coil.[11, 13] It is important to maximize this effective coil sensitivity for an imaging experiment. Thus, coils are designed for specific imaging applications to maximize the sensitivity and to minimize the noise received from areas outside the region of interest. As the region of interest becomes smaller, the amount of sample noise received decreases, and eventually the noise is dominated by thermal noise in the copper of the RF coil. Thus, small copper-loss dominated surface coils are designed to maximize the B-field while minimizing the coil resistance. If the geometry of the coil cannot be further optimized, then it would seem that the SNR of the surface coil cannot be further improved.

1.5 Cryo-Cooled Surface Coils

To push past this limit, studies have demonstrated that SNR gains can be made by using cryogenics to reduce the thermal noise generated in the RF coil. Some studies have simply cooled conventional copper coils to gain an SNR improvement, limited to an SNR improvement factor of around 2.5.[14-17] Other studies have used high-temperature superconducting (HTS) surface coils to make even greater SNR gains.[18-23] Depending on the extent of sample loading, however, HTS coils may offer only marginal gains over the performance of cryo-cooled copper coils. An excellent review paper by L. Darrasse recounts many of the various studies of cryogenic RF probes in MRI.[24]

1.6 SEA Imaging and Planar Pairs

An ongoing field of research in our lab is in the area of rapid, highly accelerated imaging. Techniques such SMASH and SENSE use arrays of coils to reduce the number of phase encoding steps needed to acquire an MR image, accelerating the acquisition of the image. Another technique, developed by our research group, employs an array of coils to eliminate the need for phase encoding.[25-30] This enables us to acquire an image with a single echo. Fittingly, the technique was dubbed Single Echo Acquisition, or SEA, imaging. SEA imaging uses a long, narrow coil to acquire each row of the image. Normal frequency encoding is used to encode spatial information in the direction parallel to the coils, and the narrow sensitivity pattern of the array elements provides selectivity in the other direction.

The array elements used for SEA imaging are planar pair coils.[31] As illustrated in Fig.1a, if unit current flows in one direction in the center conductor, the outer conductors each carry half unit current in the opposite direction. The center conductor is coupled to the coax center conductor through a matching network, and the outer conductors are connected to the coaxial shield. This element design has a very narrow sensitivity pattern, concentrated directly below the coil, and it has inherently low coupling to adjacent elements.[25] These qualities make it an excellent candidate for SEA imaging. The inherent decoupling of the planar pairs simplifies the multi-channel receiver by allowing the use of low-cost preamplifiers instead of more expensive decoupling preamplifiers. Unfortunately, this property also makes it difficult to couple to the coils inductively; so far, direct coupling has been employed with varactor tuning and matching networks.

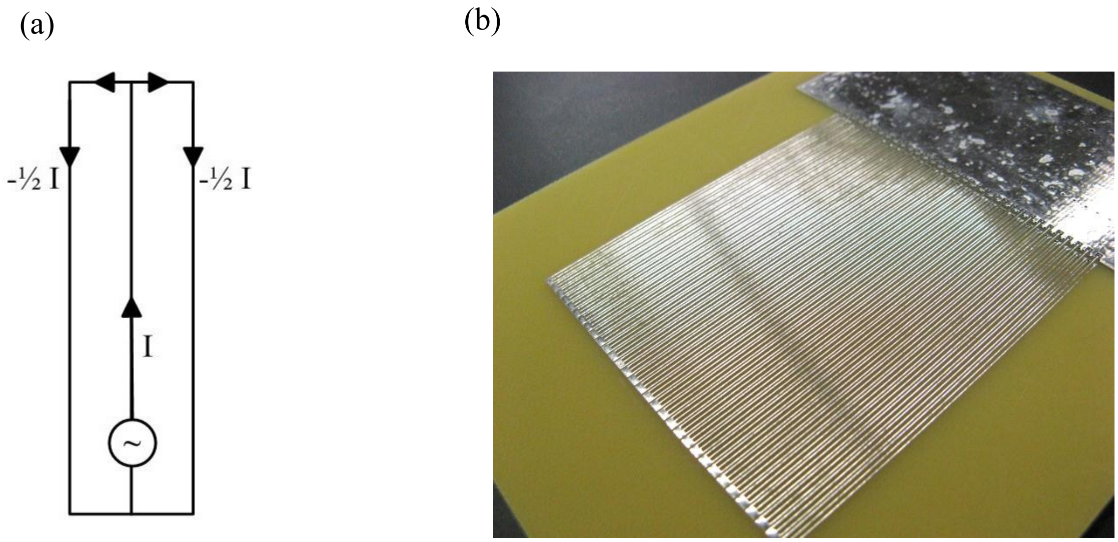

Fig. 1 Diagram of current flow in a planar pair coil (a). Photograph of a 32-channel planar pair coil array for SEA imaging (b).

SEA imaging is a technique focused on rapid imaging, with theoretical speeds approaching 1000 frames per second.[25] The number of elements in the array determines one dimension of resolution in a SEA image. The other dimension is determined by the frequency encoding; increasing readout resolution will linearly decrease the image SNR.

Thus, any increase in the SNR due to cryo-cooling will allow higher resolution in the readout direction without changing imaging speed.

1.7 Microcoils in MRI and MR Spectroscopy

For high resolution microscopy or mass-limited spectroscopy, standard surface coils may not be sufficient to recover SNR in a reasonable amount of time. For small samples and high-resolution imaging, it is necessary to continue to shrink the size of the coils. In his 1997 MR microcoil review paper, A. G. Webb acknowledges that the definition of a "microcoil" is somewhat arbitrary; he defines it as a coil with a sensitive volume of 1 μL or less, with the caveat that somewhat larger coils can be analyzed with similar principles.[32] Mcfarland and Mortara define a microcoil as having a radius less than 1 mm.[15] By these definitions, the coils studied in this thesis would barely be considered microcoils. Nevertheless, the same principles apply.

Early work in MR microcoils focused on solenoidal microcoils.[33-37] This technique is especially useful for NMR spectroscopy of fluids in capillaries. The solenoidal microcoil can be formed around a capillary tube, creating extremely high sensitivity for a very small volume. The challenge for NMR microspectroscopy is susceptibility matching: the small differences in magnetic susceptibility between the coil, capillary, and sample can cause artifacts, which can mask the useful information. Thus, much work has gone into susceptibility matching[38] and other techniques to improve the linewidth of NMR spectra with solenoidal microcoils.

For mass-limited fluidic samples, solenoidal microcoils are an attractive option with very high sensitivity and excellent spectral resolution after susceptibility correction. However, they are difficult to mass-produce, most solenoidal microcoils are hand-wound by researchers and the experimental setups are fragile and unwieldy. In addition, many applications are not well-suited to capillary tubes. For example, surface imaging cannot be accomplished effectively with a solenoidal coil, and lab-on-a-chip applications are difficult to integrate with solenoidal coils.[39] Thus, other microcoil geometries have been investigated. Planar spiral microcoils are of particular interest.

Planar spiral inductors have been used in RF applications for many years. Various geometries of these inductors (hexagonal, octagonal, rectangular, and circular) have been modeled and characterized,[40-42] and fabrication methods have been streamlined.[43] While the sensitivity of a planar microspiral coil is not as high as that of a similarly sized solenoidal microcoil, the planar geometry of the microspirals lends itself to applications for which solenoids are impractical. They are an obvious choice for surface imaging, and can easily be built into lab-on-a-chip systems.[44] Thus, researchers have investigated NMR spectroscopy[39, 45-52] and MRI[53-59] applications of planar microspiral coils, including efforts to characterize and optimize the SNR of planar microcoils.[60] The principal criticism of planar microcoils is the reduced sensitivity compared to solenoidal microcoils, which limits the achievable SNR. In addition, the series resistance is often high, reducing the coil Q and image SNR. Massin, *et al*. has identified the high series resistance of copper planar coils as a limiting factor for the SNR.[47] His research has focused on optimizing the geometry of the microspirals to increase their Q and SNR, with encouraging results. We have taken this a step farther by cryo-cooling copper microspiral coils of similar design to Massin’s, further reducing the series resistance and thermal noise generated in the coil. The theoretical and actual performance increases due to cryo-cooling are discussed in subsection 2.6.

1.8 Inductive Coupling

One final aspect of this research that deserves introduction is the inductive coupling of RF coils. Just as an NMR signal from atomic nuclei can be coupled inductively to an RF coil, a signal in one coil can be coupled inductively to other coils. Generally, inductive coil-to-coil coupling is undesirable. For instance, in a phased array coil, precautions must be taken to decouple the array elements from one another.[10] Similarly, when using a volume coil for excitation and a surface coil for detection, it is necessary either to decouple the two coils or to detune each coil when not in use.

However, it is possible to use the mutual inductance between two coils advantageously. The NMR signal can be detected with a local coil (primary coil) in close proximity to the region of interest, and then coupled inductively to a secondary coil, which is then coupled to a transmission line. This technique is referred to inductive coupling. Motivations for inductive coupling include the reduction of dielectric losses in the sample,[61, 62] isolation from ground,[63, 64] and freedom of placement of the primary coil. For instance, inductive coupling has been used for implantable probes in animals, allowing researchers to conduct multiple microscopy or spectroscopy experiments on kidneys, with higher resolution and SNR than could have been achieved from outside the body.[65, 66] While inductive coupling will degrade SNR to some degree (compared to a lossless direct coupling mechanism), it has been proven that this degradation is minor if a high-Q secondary coil is used and sufficient coupling is achieved.[61, 67-69] In practice, the inductively coupled SNR often exceeds the directly coupled SNR, due to the aforementioned reasons.

Generally, inductive coupling is used with larger surface coils for localized imaging such as spine or organ imaging, but recently it has been extended to microcoils. Sakellariou and Jacquinot have used inductive coupling to conduct a magic angle spinning experiment with a solenoidal microcoil wrapped around a capillary tube.[69, 70] In 2009, Utz and Monazami monitored flow in a capillary with a solenoidal microcoil resonator placed inside of a commercial NMR probe.[68] Both of these studies used concentric solenoids to achieve strong coupling between the primary and secondary coils. However, in the conclusion of his 2009 paper, Utz expressed a desire to extend his work in inductive coupling to planar microcoils, stating, “The main challenge lies in the design and efficient microfabrication of integrated planar microcoil resonators with sufficient coupling and Q.” Since then, his research group has presented several posters[71-73] and an oral presentation,[74] presenting a variety of inductively coupled planar microcoils, including Helmholtz pairs, self-resonant microspirals, and microspirals resonated with interdigitated finger capacitors.

2. PLANAR PAIR COILS

2.1 Introduction

In fall 2010, the project was in its later stages. At that time, work was ongoing on cooling planar pair coils used by our research group for an imaging technique called single echo acquisition, or SEA, imaging. Before the cryo-cooling tests could be completed, however, a method for accurate bench testing of Q had to be developed and tested due to variability observed in previous measurements. After developing this methodology, planar pair coils were manufactured and bench tested. Then images were acquired and the SNR improvements compared to predictions. This section of the thesis will cover both the Q testing approach and the planar pair coil imaging methodology and results.

2.2 Developing Accurate Reflection-Type Q Measurements

2.2.1 The Importance of Q Measurements

In this research, Q measurements play an important role as they are used to determine the relative lossiness of a resonated coil. The Q of a coil can be expressed as the ratio of reactance to resistance: $Q = \frac{\omega L}{R}$. Thus, if the inductance of the coil is known, the equivalent resistance can be determined from an accurate Q measurement. Even if the inductance is unknown, Q measurements can reveal the relative resistance of the coil after cryo-cooling. This is valid since inductance is a function of geometry and changes very little upon cryo-cooling. Furthermore, because resistance in the coil is responsible for SNR-limiting thermal noise, Q measurements are extremely useful for determining the expected SNR gain due to cryo-cooling. While it is often stated that $SNR \propto 1/\sqrt{Q}$, this is only true if the coil resistance changes, and other factors (such as temperature) remain constant. The cryo-cooling SNR performance and its relationship to Q measurements are discussed more fully in subsection 2.6.

2.2.2 Measuring Q

The Q of a resonated coil is defined as the ratio of the energy stored (in the inductor and resonating capacitor) to the energy lost (in the resistance of the coil) per cycle. This is proportional to the ratio of the inductance to the coil resistance, as observed previously. However, this can also be seen in the frequency response of the resonated coil. It is commonly observed that the bandwidth of a resonator is given by: $\Delta f = \frac{f_0}{Q}$, where Δf is the half power bandwidth and f_0 is the center frequency of the resonator. Thus, the Q of MRI coils is generally measured with transmission-type measurements. Specifically, two decoupled probes are brought close to a coil, and an S_{21} measurement is taken with a network analyzer. From this transmission measurement, f_0 and Δf can be determined, and Q calculated.

2.2.3 Appeal of a Reflection (S_{11}) Type Measurement of Q

Unfortunately, the geometry of planar pair coils makes this S_{21} measurement very difficult. The magnetic flux from the electrical currents in the two loops cancels out quickly when moving away from the coils. Thus, the measurement would require very small probes, brought very close to the coil. While this is sometimes possible, it is inconvenient and impractical. This is especially true when the coil is affixed to the phantom and the microfluidic polymer channels, because there is no free direct approach to the coil. Thus, there is great motivation to make Q measurements through reflection-type (S_{11}) measurements. S_{11} measurements are already used to verify the matching and tuning of the coil. (Generally return loss should be 20 dB or greater at f_0.) It is also clear that bandwidth can be measured from the return loss plot; thus, a Q measurement should be possible. However, it was unclear what return loss should be used for the bandwidth to calculate Q.

2.2.4 Literature Search

Scant literature was found on the subject of simple reflection-type Q measurements. One conference lecture was found that referenced the 7 dB return loss bandwidth, but it offered no theoretical explanation.[75] However, on page 329 of *Foundations for Microwave Engineering*, Robert Collin claims that, "For circuits with a loaded Q of 5 or more, the frequency response is very nearly the same as that of a parallel RLC circuit, over the useful operating frequency band. Thus, the 3-dB fractional bandwidth is $1/Q_L$. For circuits with a low Q, the frequency behavior is different but similar." [76] When Collin refers to the loaded Q, he is referring to the Q of the circuit including a matching network and 50 Ω load. $Q_L = Q/2$, because when the circuit is matched to a load, half of the power is transferred to the load.

This statement is useful because it allows any resonant circuit with a loaded Q of five or more to be treated as a simple RLC circuit. Thus, Collin's expression for input admittance,

$$Y_{in} \approx Y_c \left(1 + 2jQ \frac{\Delta\omega}{\omega_0}\right)$$

is used to calculate the return loss at the appropriate fractional bandwidth to measure the unloaded Q. $Y_C = 1/50$ is used as the value of the characteristic line admittance.

Next, $Q = \frac{\omega_0}{2\Delta\omega}$, the assumption that associates the Q measurement with the fractional bandwidth, is plugged in. (Note that Collin refers to the bandwidth as 2Δω, instead of simply Δω.) This gives:

$$Y_{in} \approx {}^{1}\!/_{50}\,(1+j)$$

Translating this to a reflection coefficient yields:

$$\rho = \left|\frac{Y_C - Y_{in}}{Y_C + Y_{in}}\right| = \left|\frac{{}^{1}\!/_{50} - {}^{1}\!/_{50}\,(1+j)}{{}^{1}\!/_{50} + {}^{1}\!/_{50}\,(1+j)}\right| = \left|\frac{-j}{2+j}\right| = \frac{\sqrt{5}}{5}$$

Calculating the equivalent return loss:

$$RL = -20log_{10}\frac{\sqrt{5}}{5} = 6.99\ dB$$

Thus, the 7 dB fractional bandwidth of return loss is the inverse of the unloaded Q of the coil. This calculation can be repeated with the loaded Q to show that the 3 dB fractional bandwidth is $1/Q_L$.

2.2.5 Numerical Verification

Because this derivation relied on the premise that the resonated and matched coil acts like an RLC circuit, it was desirable to verify this assumption numerically for our coils. The planar pairs used in this research can be roughly approximated (at 200 MHz) as a 60 nH inductor and a 2 Ω resistor in series. (Q = 38) A MATLAB® script (included in appendix A) was written to compare the frequency response of the matched and tuned coil to an equivalent parallel RLC circuit (R = 50 Ω, with L and C to resonate at 200.1

MHz with the same Q as the coil). Fig. 2 shows the reflection coefficient (negative of return loss) vs. frequency of the matched and tuned coil, plotted over the return loss of the equivalent RLC circuit. The plot demonstrates that there is very little deviation from the parallel RLC model. Thus, measuring the 7 dB return loss fractional bandwidth is theoretically an excellent technique from which to calculate the Q of a coil. In addition, this numerical technique can easily be used to verify whether this approximation is applicable on other coils, given a rough estimate of the coil resistance and inductance.

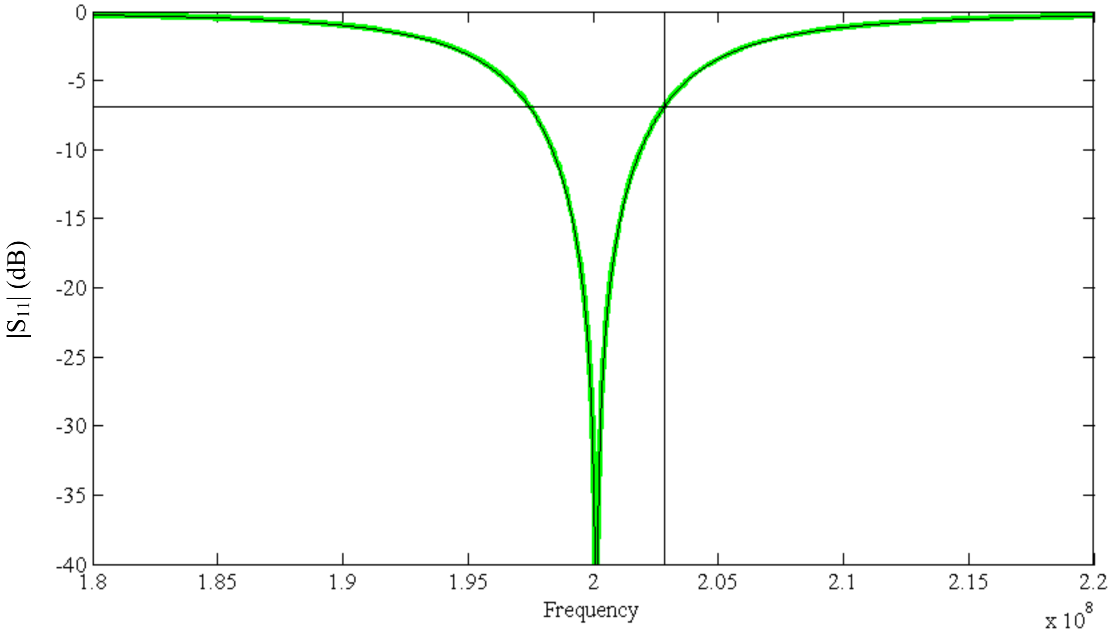

Fig. 2 S_{11} magnitude of an equivalent parallel RLC circuit (broad line, green) and a matched and tuned SEA coil (thin line, black) vs. frequency around the resonant frequency of the circuits. Horizontal line shows at -7 dB shows where the fractional bandwidth would be measured to calculate Q of the circuit.

2.2.6 Experimental Verification

Finally, the 7 dB return loss Q measurement technique was compared to the standard dual probes Q measurement on a larger coil to demonstrate the equivalence of the two techniques. Q measurements were taken with both methods on an 8 cm diameter copper surface coil over a saline phantom. The coil was tuned and matched with a fixed ceramic capacitor (American Technical Ceramics, Huntington Station, NY) and two variable capacitors (Voltronics Corporation, Denville, NJ). Varactors were not used for this test because they can add losses that change with biasing voltage. Fig. 3 shows the coil and matching network.

Fig. 3 Coil (8 cm diameter) and matching network used for validation of 7 dB return loss Q measurement.

Fig. 4 Coil, matching network, and balun test setup for S_{11} 7 dB return loss measurement.

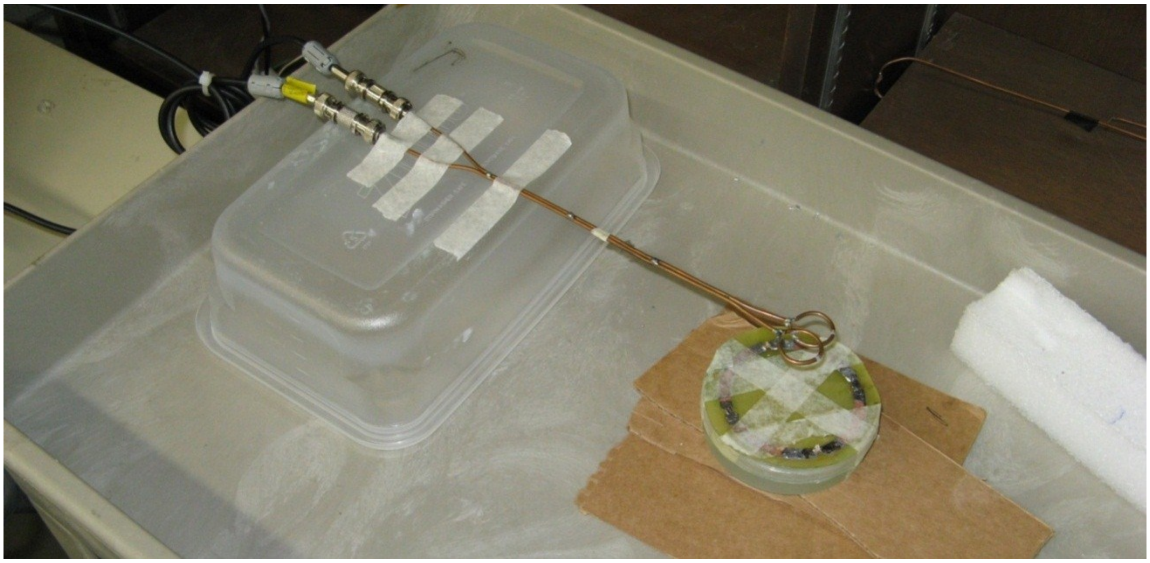

Fig. 5 Coil resonated with fixed capacitors, with the matching network removed. Dual probes are used to measure Q with an S_{21} transmission-type measurement.

The Q was measured three ways: 1) 7 dB return loss method (see Fig. 4), 2) S_{21} dual probes with the matching network attached to the coil, but open circuited, 3) S_{21} dual probes with no matching network – fixed capacitors only (see Fig. 5). This third measurement type was added because it was observed that the matching network added some losses. To validate the reflection-type measurement across a range of Q factors, various values of thin film resistors (0, .275, .5, 1, 2, 4.3, and 7.5 Ω) were soldered in line with the coil to reduce its Q in a known fashion.

The data from this experiment shows some discrepancy due to the losses in the matching network. The results, shown in Fig. 6, show that the Q factor measured with the S_{11} 7 dB method lies between the measurements with the dual probes. The dual probes measured a higher Q when the coil was resonated with only a fixed cap. It seems that the addition of the open circuited matching network added considerable loss. However, as more resistance is added, all three measurements converge as the resistance added to the coil becomes dominant over any losses due to the matching network. Although not pictured, it is interesting to note that if the matching network is terminated in a 50 Ω load, the Q measured with the dual probes method is half of the open-circuited Q value. This is the "loaded Q" that was referred to in the Collin reference.

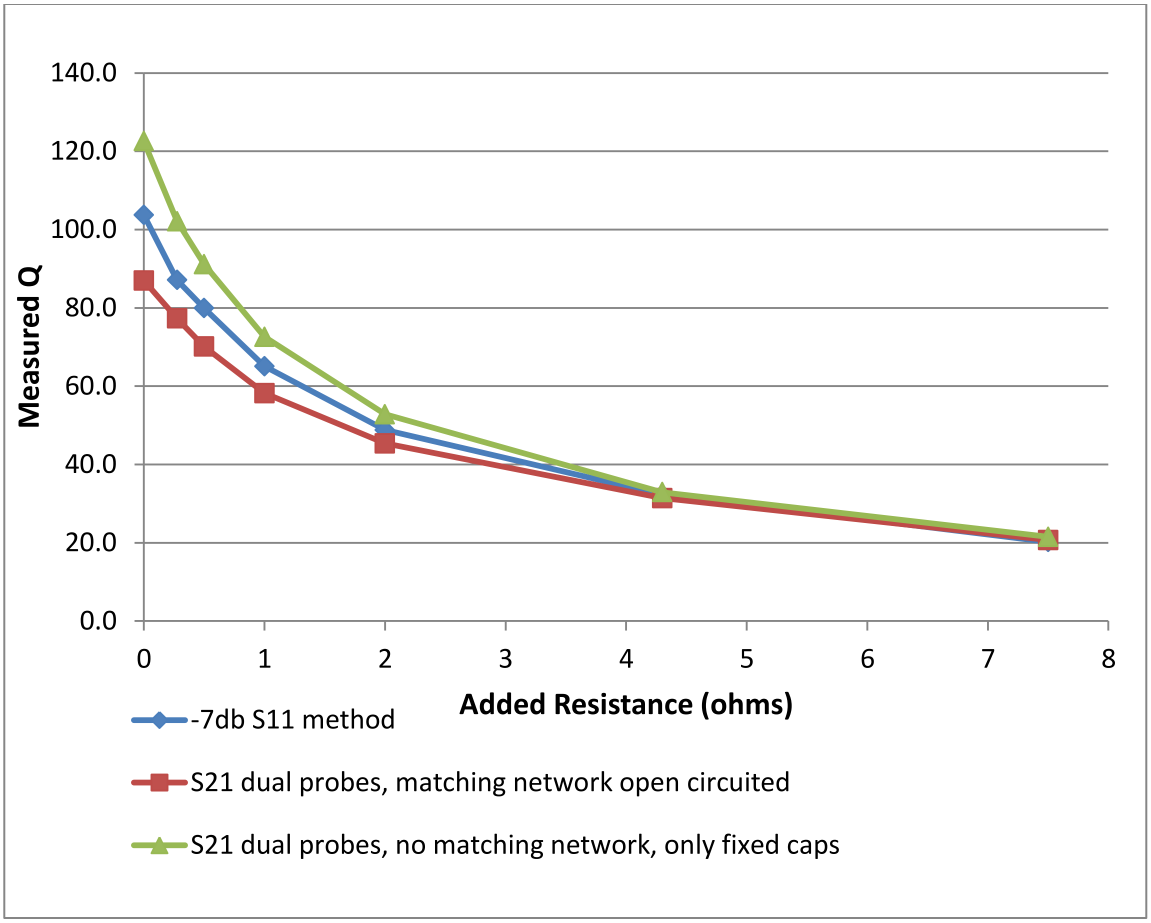

Fig. 6 Comparison of dual probe Q measurements to S_{11} reflection-type measurement. Data converges as added resistance increases.

2.2.7 Conclusions on Reflection-Type Q Measurements

The 7 dB return loss method of measuring Q is a valuable tool for measuring the Q of coils without perturbing the system. It did not completely correspond with one of the dual probes Q measurements, but it showed a trend consistent with that of the more traditional measurements. The fact is, every Q measurement changes the loading of the system to some degree. The 7 dB return loss method is an excellent, theoretically sound method that can be used to measure the Q with loading conditions nearly identical to those when imaging. Specifically, the coil is attached to the phantom and matching network as it is during imaging, and the coil is not perturbed by any external probes. Furthermore, this Q measurement is well suited for this research, because the primary concern is with Q ratios, not absolute Q values. Therefore, unless otherwise specified, the rest of the Q measurements in this thesis have been acquired using the 7 dB return loss method.

2.3 Manufacturing Planar Pair Coils

2.3.1 Previous Planar Pairs

As mentioned in the introduction, MRSL has conducted research using an array of planar pair coils to acquire an image with a single echo.[25-30, 77, 78] This technique is called "Single Echo Acquisition" imaging, or SEA imaging. Thus, planar pairs are often referred to as "SEA coils." In the past, SEA coil arrays have been manufactured in-house on standard FR-4 and flexible substrates. At other times, the coil fabrication has been outsourced commercially to obtain highly precise samples. Previously, flexible substrates have been investigated for the possibility of conformable arrays. However, cryo-cooling of these arrays has not been explored. Due to the conflicting constraints imposed when cryo-cooling coils with limited imaging depth, it was desirable to manufacture planar pair coils on a thin substrate, yet one with a low thermal conductivity. Through a partnership with Dr. Arum Han of the NanoBio System Laboratory, (Electrical and Biomedical Engineering, Texas A&M University), microfabrication techniques have been introduced to this work. Chiwan Koo, one of Dr.

Han's students, has aided greatly in this work by microfabricating coils on various substrates. This has diversified the planar pair work and avoided some of the restrictions of traditional coil fabrication. However, it was necessary to verify that the microfabricated coils had similar performance (Q) to etched copper coils, so equivalent samples were fabricated using both methods for comparison.

2.3.2 Traditional Mechanically Etched Planar Pair Coil

A planar pair coil was etched out of 35 µm thick copper on a standard FR-4 substrate. The coil (Fig. 7) was 5.7 cm long, with 10 mil (254 µm) trace width and 20 mil (508 µm) trace separation. Due to limitations of the current microfabrication process, the length chosen was shorter than the SEA coils used in our previous research. However, the 5.7 cm length is sufficient for proof of concept. Matching network pads were fabricated on the same substrate for variable capacitors (Voltronics Corporation, Denville, NJ).

Fig. 7 CAD layout for mechanically etched planar pair coil. The matching network pads are the appropriate size for variable Voltronics capacitors.

Two coils were etched on the substrate but only one was used. The coils were etched using a PC board prototyper (C30, LPKF, Wilsonville, OR). After etching, excess copper foil was removed from the substrate by hand, the variable capacitors were soldered to the matching network pads manually and a coaxial cable connection was attached. Fig. 8 shows the final assembly of the machine-etched SEA coil.

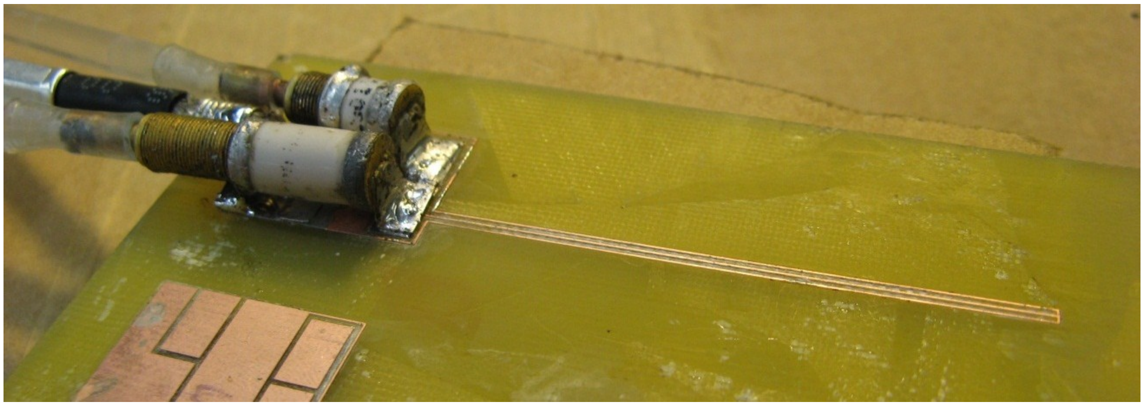

Fig. 8 Machine-etched SEA coil with Voltronics variable capacitors and coaxial connection.

2.3.3 *Microfabricated Planar Pair Coils*

Various microfabricated SEA coils were fabricated by Chiwan Koo using the facilities of the NanoBio Systems Lab, MRSL, and Electrical and Biomedical Engineering Department resources. For this comparative study, coils were fabricated on a .5 mm thick poly(methyl methacrylate) (PMMA) substrate. PMMA was chosen for its strength and low thermal conductivity (0.17 W/mK) compared to silicon (1.6 W/mK) or glass (1.1 W/mK). This property helps to minimize the coil-to-sample distance and isolates the imaging surface from the extremely low temperature of liquid nitrogen (77

K). Koo's coils were fabricated by copper electroplating on chromium and copper films, using photolithography to define the coils. For details on the fabrication process, see Koo's works.[79, 80] Dimensions of the microfabricated coil were the same as the machine-etched coil, except that the copper electroplating thickness was generally targeted for 25 μm. However, one coil was intentionally microfabricated with a 1 μm thickness. This thin coil was used to demonstrate the different behavior seen in coils thinner than one skin depth after cryo-cooling.

2.4 Matching Networks

Variable capacitors (Voltronics Corporation, Denville, NJ) were used to match and tune the machine-etched SEA coil (see Fig. 8). These variable capacitors are adjusted by turning a threaded rod, which modifies the overlap of plates inside of the capacitor. These capacitors were soldered onto pads etched on the same substrate as the coil. The microfabricated coils did not have an integrated matching network. Instead, a daughter board designed by Ke Feng, one of Dr. Wright's students who previously worked on this research, was soldered to the board (see Fig. 9). This board consists of two high-Q varactors (Microsemi, Irvine, CA) for matching and tuning, ceramic capacitors (American Technical Ceramics) to bias and isolate the varactors, and thin film resistors to prevent DC blocking to the varactors. The matching varactor is biased over the RF line and an extra DC connection was added to bias the tune varactor. Fig. 10 shows schematic diagrams of the variable capacitor matching network (a), and the varactor matching network (b).

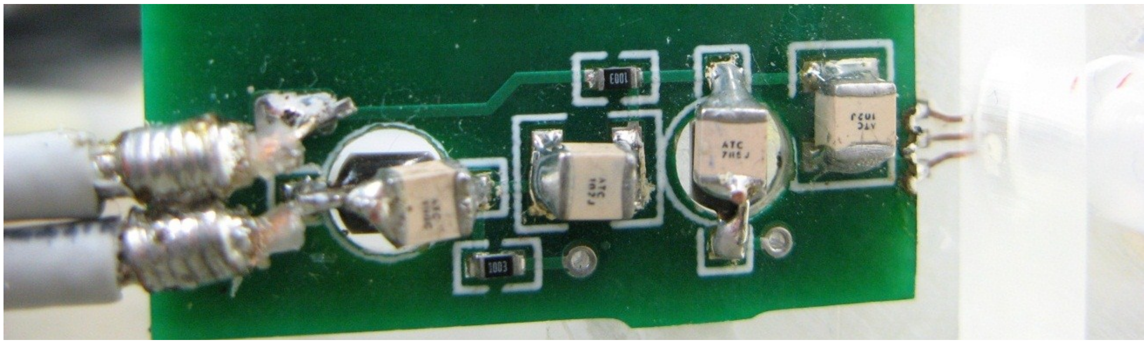

Fig. 9 Daughter board (designed by Ke Feng) used for matching and tuning microfabricated coils. The varactors are underneath the ceramic capacitors.

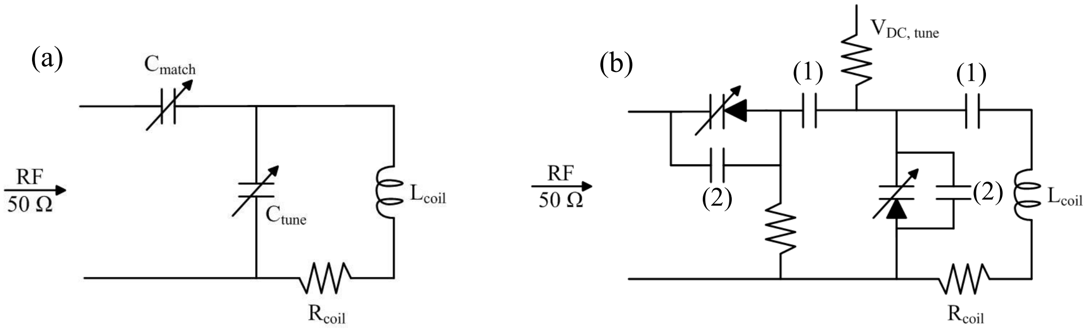

Fig. 10 Schematic diagram of variable capacitor matching network (a); Schematic diagram of varactor matching network (b). Capacitors labeled (1) are high value DC blocking capacitors, typically 1 nF or greater. Capacitors labeled (2) are added in parallel with the varactors to permit adjustment of DC biasing.

Both types of matching networks have distinct advantages. Matching and tuning with varactors requires a more complicated circuit and two DC power supplies. However, varactors allow the circuit to be adjusted by merely changing the DC voltages; no physical interference is required. This is a distinct advantage when comparing the SNR of a coil before and after cryo-cooling as it is important that the system remains stationary for an accurate comparison. On the other hand, the varactors inevitably add more loss (and therefore noise) to the system, due to their high equivalent series resistance (ESR). The ESR of varactors decreases as the biasing voltage is increased, making it desirable to use the varactors at a relatively high voltage to minimize losses. Varactor performance is more fully analyzed in subsection 3.2.3.

2.5 Bench Testing Planar Pair Coils

Bench tests are essential to confirm that the coil assembly is ready for an imaging test, before the magnet is reserved and the other necessary preparations made. Thus, the Q factors of the machine-etched and microfabricated coils were measured on the bench using the 7 dB return loss method, both at room temperature (RT) and cryo-cooled temperature (LT). Coils were cryo-cooled by feeding liquid nitrogen through microfluidic polymer channels attached to the coil substrate. For bench testing, liquid nitrogen was introduced using a gravity-fed method. Fig. 11 shows a photograph of the 35 µm copper coil being cryo-cooled during this phase of testing. The microfluidic cooling channels were constructed out of Poly(dimethylsiloxane) (PDMS, thermal conductivity = 0.18 W/mK) (Sylgard 194, Dow Corning., Midland, MI) using a soft lithography process.[81] The coil substrate had a layer of PDMS applied, via the spin coating method, to serve as an adhesive for attaching the microfluidic channel structure.

Fig. 11 35 µm copper etched planar pair coil with PDMS microfluidic channel attached. The coil is being cryo-cooled by gravity-fed liquid nitrogen through the PDMS channel. Ice formation is evident on the liquid nitrogen inlet.

An HP 4195A vector network analyzer was used in S_{11} mode to take this measurement. The machine-etched coil was tuned and matched by adjusting the capacitance of the Voltronics variable capacitors to maximize return loss at 200.1 MHz. Likewise, the microfabricated coils were tuned and matched by adjusting the biasing voltage to the varactors. Generally, 30 dB or greater return loss was considered “matched,” for Q measurements and imaging. In the case of the varactor-tuned coil, the ceramic capacitors in parallel with the varactors were changed as necessary to allow the coil to be tuned and matched at both RT and LT, and to maximize Q as much as possible. Table 1 shows results of bench tests comparing the performance of the mechanically etched coil and the microfabricated coils.

Table 1 Results of bench testing of various planar pair coils. Voltages are given for coils matched and tuned with varactors. Other coils are tuned and matched with Voltronics variable capacitors.

	Q – 35 μm Cu etched	Q – 22 μm microfab	V_{Match}	V_{tune}	Q – 1 μm microfab
RT	35.1	30.9	2.85	2.7	10.9
LT	67.6	52	4.6	1.4	32.9
Average Q improvement:	1.93	1.68			3.02

The Q increased by a greater factor after cryo-cooling the Voltronics-tuned coil. This is not surprising, because the voltages used to bias the varactors were so low. Low biasing voltages result in higher ESR, causing increased losses in the varactors. In future tests, higher biasing voltages were used to reduce the losses. Note that while the absolute Q factor of the 1 μm thick coil was much lower, the increase due to cryo-cooling was much higher than the other coils due to the absence of the skin effect. This phenomenon will be discussed more thoroughly in subsection 2.6.3.

These preliminary Q measurements showed that the microfabricated coil performs nearly as well as the traditionally etched coil. If the varactors are tuned at the higher voltages, the Q's should be even closer. However, conditions change when the coil is attached to a phantom and loaded into the bore of the magnet. Thus, these Q measurements were not used to predict SNR improvement of individual imaging experiments. Instead, Q measurements were taken at the time of imaging, right after the coil was tuned and matched to the Larmor frequency inside the bore of the magnet (subsection 2.7).

2.6 Planar Pair Noise Modeling

2.6.1 Thermal Noise in Conductors

In loaded volume coils, noise from the sample generally exceeds coil noise. This can be quantified by measuring the Q of the volume coil with and without the sample inside. Just as electrical resistance is proportional to noise in the copper, lossy tissue will generate noise in the MR signal. This drop in Q is quantified as: [17]

$$\frac{Q_L}{Q_U} = \frac{R_{Coil}}{R_{Coil} + R_{Sample}}$$

In the case of a volume coil, it is desirable to see a significant decrease in Q after loading, as this indicates that the coil is not contributing significant noise. However, in the case of small surface coils and microcoils, the sample loading is very low, and the dominant noise source becomes the coil resistance. For the planar pairs and microspirals in this research, virtually no change in Q was observed due to loading.

Thus, the noise in our microcoils can be attributed solely to resistances in the coil, interconnects, and matching network. Nyquist describes the mean square voltage noise in a conductor as follows: [82]

$$\langle V \rangle^2 = 4k_b T R \Delta f$$

where k_b is Boltzmann's constant ($1.38\text{x}10^{-23}$ J/K), T is the absolute temperature of the conductor, R is the resistance in the conductor, and Δf is the frequency bandwidth of the measurement.

2.6.2 Thermal Noise and SNR

Because thermal noise is the dominant noise source, the SNR of an MR experiment is proportional to the inverse of the square root of temperature and resistance:

$$SNR = \frac{V_{Signal}}{V_{Noise}} = \frac{V_{Signal}}{\sqrt{4k_b TR\Delta f}} \propto \frac{1}{\sqrt{TR}} \propto \sqrt{\frac{Q}{T}}$$

Generally, the bandwidth and signal voltage can be treated as constant for the purposes of this research. While it is often quite difficult to accurately measure the resistance of a coil assembly at the frequency of interest, measuring Q is generally straightforward. Because Q is inversely proportional to coil resistance, the SNR improvement due to cryo-cooling can be expressed as:

$$\mathrm{SNR}_{\mathrm{improvement}} = \frac{SNR_{cooled}}{SNR_{room}} \sqrt{\frac{\mathrm{T}_{\mathrm{room}}/\mathrm{Q}_{\mathrm{room}}}{\mathrm{T}_{\mathrm{cooled}}/\mathrm{Q}_{\mathrm{cooled}}}}$$

2.6.3 The Skin Effect

When copper is cooled from room temperature (295 K) to liquid nitrogen temperature (77 K), its resistivity drops approximately by a factor of 8.[83] While the DC resistance of a copper conductor will thus be reduced 8 times after cryo-cooling, the reduction in high frequency resistance is limited by the skin effect. The skin depth can be described as:

$$\delta = \sqrt{\frac{2\rho}{\omega\mu}}$$

where ρ is the resistivity of the conductor, ω is the angular frequency of the current, and μ is the magnetic permeability of the conductor. If the resistivity is decreased by a factor of 8, the skin depth will be reduced by a factor of $\sqrt{8} \cong 2.83$, decreasing the effective conductor area. Thus, the high frequency resistance will be only decrease by a factor of $\sqrt{8} \cong 2.83$. This rule only applies if the conductor dimensions are large compared to the skin depth. The skin depth of copper ($\rho = 1.68\text{x}10^{-8}$ Ωm) at RT is about 4.61 μm, falling to 1.63 μm at LT. Generally, coils are manufactured with dimensions much larger than the skin depth to maximize the Q, but one thin coil (1 μm thickness) was manufactured to observe the differences. As expected, the Q increase was more dramatic in the 1 μm coil (see Table 1 and subsection 2.5).

2.6.4 Theoretical and Actual Cryo-Cooling Performance

Therefore, assuming coil dimensions are large compared to the skin depth and that sample loading is negligible, the ideal SNR improvement attainable by cryo-cooling a copper coil is: [17]

$$\mathrm{SNR_{improvement}} = \sqrt{\frac{\mathrm{T_{room}}/\mathrm{Q_{room}}}{\mathrm{T_{cooled}}/\mathrm{Q_{cooled}}}} = \sqrt{\left(\frac{295}{77}\right)2.83} = 3.3$$

This establishes an absolute maximum SNR improvement for liquid nitrogen cooling of copper coils. This is quite significant – a 3.3 times increase in SNR would allow an 11 times decrease in imaging time to achieve comparable images. Higher improvements could be gained by using helium to cryo-cool the coils to a lower temperature, or more likely, by using HTS coils.

Unfortunately, this theoretical maximum improvement was not achievable with the defined experimental setup. The above equation assumed that all conductors contributing resistance were cooled to 77 K. In the given setup, the interconnects and matching network were not cryo-cooled. Any resistances not cooled detract from the ideal Q increase of 2.83 (including ESR in the varactors). Furthermore, uncooled resistances continue to contribute noise at the higher temperature. The fractional portion of resistance at RT due to the coil can be determined from the Q improvement according to:

$$\frac{R_{coil,room}}{R_{coil,room} + R_{match}} = \frac{1 - {}^{Q_{RT}}/_{Q_{LT}}}{1 - \sqrt{{}^{1}/_{8}}}$$

where $R_{coil,room}$ is the resistance of the coil at room temperature, and R_{match} is the resistance contributed by the matching network. This can be derived from the following equations:

$$Q_{RT} = \frac{\omega L}{R_{coil,room} + R_{match}} \quad and \quad Q_{LT} = \frac{\omega L}{\sqrt{{}^{1}/_{8}}\, R_{coil,room} + R_{match}}$$

Similarly, the fractional portion of resistance at LT due to the coil can be determined as:

$$\frac{R_{coil,cold}}{R_{coil,cold} + R_{match}} = \frac{\sqrt{{}^{1}/_{8}}\left({}^{Q_{LT}}/_{Q_{RT}} - 1\right)}{1 - \sqrt{{}^{1}/_{8}}}$$

Finally, it is possible to extend these calculations to predict the SNR improvement given the observed Q increase after cryo-cooling.

$$\frac{SNR_{LT}}{SNR_{RT}} = \sqrt{\frac{(Q_{LT})295}{Q_{RT}\left(\frac{(R_{coil,cold})77 + (R_{match})295}{R_{coil,cold} + R_{match}}\right)}}$$

This is a modified version of the simple SNR improvement expression mentioned first in this subsection. The denominator accounts for the distribution of the resistances at different temperatures.

As a practical example, consider a factor of 1.8 Q improvement, similar to that observed in our experiments. From this measurement, we can calculate that 69% of the resistance is in the coil with the whole system at room temperature. After cryo-cooling, of the coil, the coil resistance is only 44% of the total resistance. Thus, the matching network is the dominant noise source by far at LT, having more resistance and higher temperature than the coil. The expected image SNR improvement is:

$$\frac{SNR_{LT}}{SNR_{RT}} = \sqrt{\frac{(1.8)295}{(.44)77 + (.56)295}} = 1.63$$

An SNR improvement of 1.63 times is still significant. This would allow for a reduction in imaging time by a factor of 2.7 or for an increase in isotropic resolution by 18%. However, the large difference between this actual performance and the theoretical maximum of 3.3 highlights the effects of even small stray resistances in the matching network and interconnects. It was not until nearly the end of the planar pair imaging and testing that the full extent of this limitation was realized. Thus, it will be analyzed and accounted for, but it may appear that we did not make adequate attempts to mitigate its effects. Later, in the research focused on microspirals, the losses due to the matching network was more fully analyzed (subsection 3.2), including evaluation of varactor performance and attempts to cool the matching network.

It is worth pointing out that any sample noise (generally neglected in this research) will have a similar effect, since the sample generally must be held at room temperature. This is expressed by A. C. Wright, *et al*. as: [17]

$$\frac{SNR_{77}}{SNR_{300}} = \sqrt{\frac{300\left(Q^{-1}_{Unloaded,300}\right) + 300\left(Q^{-1}_{Sample}\right)}{77\left(Q^{-1}_{Unloaded,300}\right) + 300\left(Q^{-1}_{Sample}\right)}}$$

2.7 Planar Pair Imaging

2.7.1 Phantom and Coil Assembly

Although details justifying the fabrication and cryogenic techniques used here are outside the scope of this thesis, it is worth mentioning that Koo and Han have published works on optimizing the cryo-cooling microchannel size, liquid nitrogen driving pressure, and nitrogen gap size in these and similar experiments.[79, 80] Pertinent details, such as dimensions, materials used, and experimental conditions are included, as well as references to literature on these subjects.

After bench testing was completed, the coil substrate was integrated with the imaging phantom. In the field of MRI, the term “phantom” is used to refer to an object that can be imaged to determine the performance of an MR system. The simplest phantom is a cavity filled with water, which can be imaged to determine the SNR of the coil configuration. A more sophisticated phantom might include fine details to test MRI resolution. For our planar-pair imaging tests, we used a simple cavity hollowed out of acrylic and filled with a 0.1% copper sulfate aqueous solution (1 g copper sulfate per 1 L water).

One acrylic block (12.5 mm thick, McMaster-Carr, Atlanta, GA) was used to create the phantom and nitrogen gap. A rapid prototyping machine (MDX-40, Roland DGA Corp., Irvine, CA) was used to remove the phantom cavity and nitrogen gap. An array of acrylic pillars were left in the nitrogen gap to prevent the hollow space from collapsing when the assembly is clamped together. A 3-foot-long acrylic board was used to support the tubing used for liquid nitrogen and gas phase nitrogen. Semicircular acrylic cradles were affixed to this board with epoxy (Loctite, Henkel Corp., Ohio). These cradles were fitted to the inner shape of the acrylic cylinder forming the body of our volume coil. The volume coil used for this research was an in-house constructed actively detuneable birdcage style coil, and was used as the transmit coil for the planar pair imaging.

To attach everything together, the planar pair coil (already bonded with the cryo-cooling microfluidic channel) was placed between the two acrylic frames; this assembly was tightly clamped using nylon screws and inserted into the volume coil. After final assembly, the total distance between the coil and the imaging surface of the phantom was 2.1 mm (0.5 mm PMMA coil substrate, 1.0 mm nitrogen gap, 0.6 mm acrylic phantom wall). Fig. 12 shows an illustration of the coil and phantom assembly. Fig. 13 shows a photograph of the assembled device. Finally, Fig. 14 shows an illustration of the volume coil and cryogenic connections.

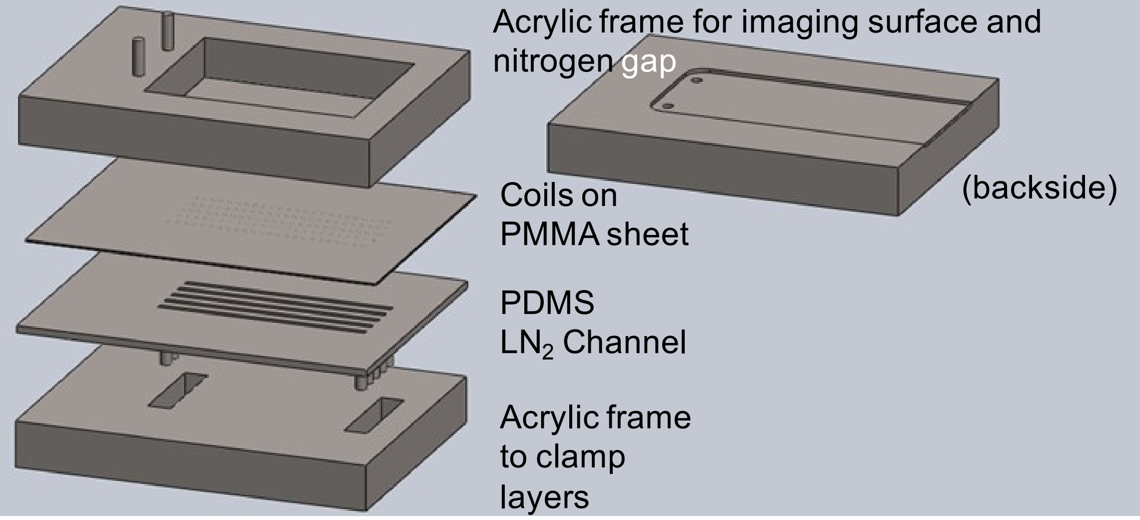

Fig. 12 Illustration of microfluidic cryo-cooling device components. The phantom is formed in the top acrylic frame piece by filling the large cavity with copper sulfate solution.

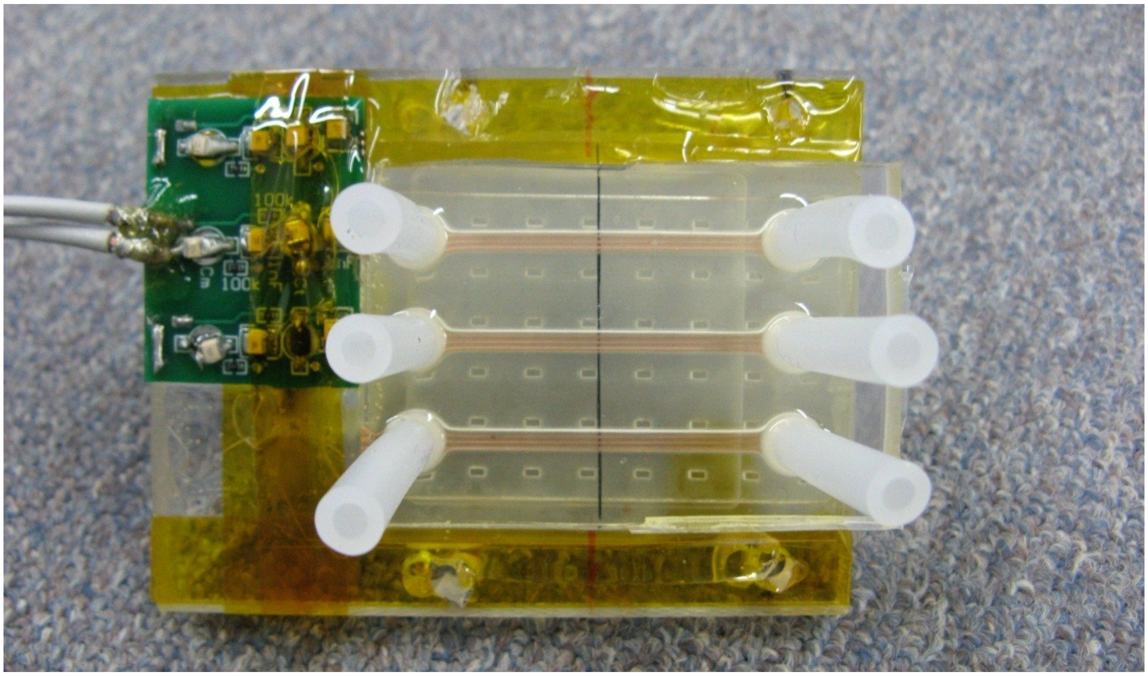

Fig. 13 Phantom and coil assembly. Three coils and microfluidic channels were fabricated, but only one was tested. Nylon pillar array is visible underneath coil substrate and microfluidic cooling channels.

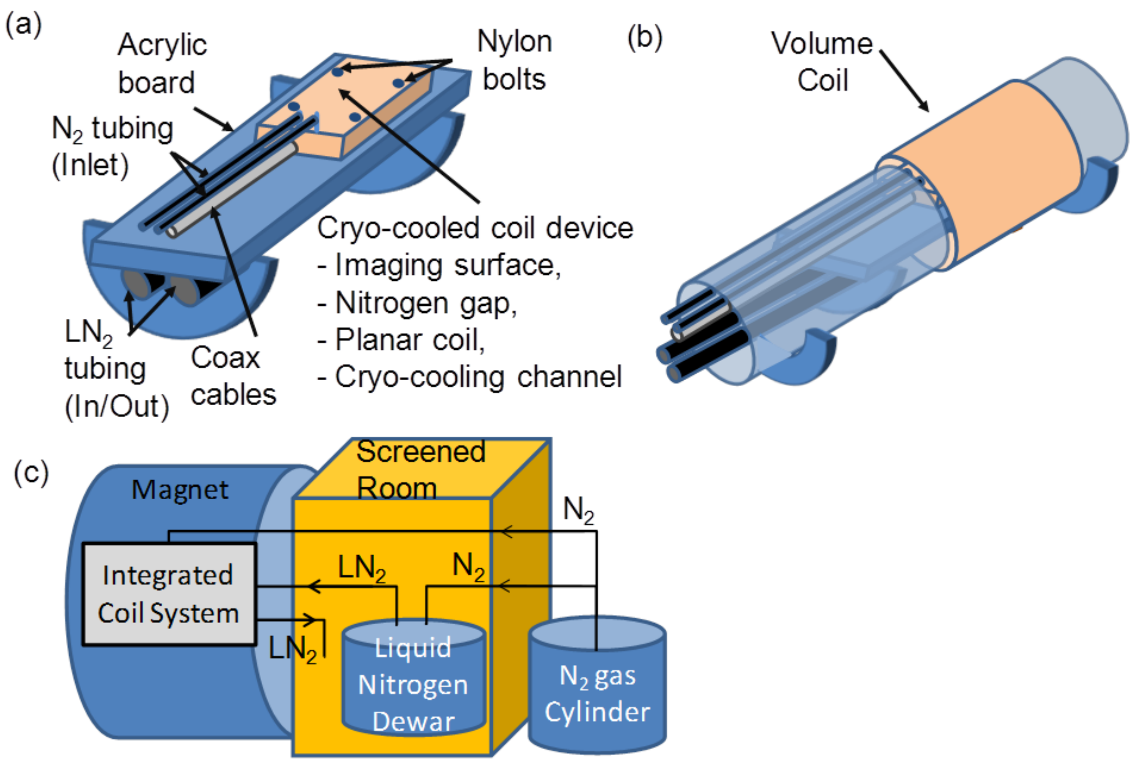

Fig. 14 Volume coil and cryogenic connections. (a) Acrylic board supporting the cryogenic tubing and coil assembly. (b) Volume coil with (a) inserted. (c) Diagram of liquid and gas nitrogen flow.

2.7.2 Imaging Procedure

The following procedure was followed in order to prepare the RT and LT experimental setup so that they could be executed back to back without disturbing the system. The imaging assembly was inserted into the 4.7 T magnet, such that the SEA coil device was centered in the bore. A 20 L pressurized Dewar was connected to the liquid nitrogen inlet tubing. A gas phase nitrogen cylinder was attached to the appropriate connections to pressurize the Dewar and supply the nitrogen gap between the coil substrate and imaging surface. Although it was necessary to leave the bore of the magnet unshielded for these fluidic connections, the liquid nitrogen source was kept inside an RF screen room to reduce potential interference. The volume coil was matched and tuned to the Larmour frequency with the use of a vector network analyzer (HP 4395).

After making all the fluidic connections, two DC power supplies were used to match and tune the coil device while monitoring the return loss via the network analyzer. A Mini Circuits bias tee was used to bias the match varactor over the RF signal line. The Q was measured using the 7 dB method and the biasing voltages were logged as well. The transmit power was calibrated using the volume coil in transmit and receive, to achieve a uniform maximum excitation. Volume coil images were also used to verify the correct positioning of the phantom inside the magnet. Next, MR images were acquired at RT using the volume coil for excitation and the planar pair coil device for receive. The volume coil was actively detuned during receive to prevent noise coupling to the planar pair. Transverse slices (perpendicular to both the imaging surface and the long axis of the planar pair coil) were acquired at the isocenter of the magnet. A spin echo sequence was employed with a matrix size of 256 x 256, TR (repetition time) of 500 ms, TE (echo time) of 50 ms, 2 averages, a slice thickness of 3 mm and a spectral width of 20 kHz.

Once the RT images were acquired, the gas phase and liquid nitrogen supplies were activated, beginning the cryo-cooling process. Due to the length of tubing between the Dewar and the coil, 30 to 40 minutes was required to fully cryo-cool the device. During this time, the coil return loss was monitored with the network analyzer, and the biasing voltages were adjusted to match and tune the coil at LT. Once the return loss stabilized and liquid nitrogen visibly flowed from the outlet, the Q of the planar coil and the biasing voltages were recorded once again. LT images were acquired using the same parameters as the RT images.

2.7.3 Imaging Results

MATLAB® was used to render images and evaluate image SNR. First, the magnitude image was reconstructed with a simple 2D Fourier transform without any corrective filter. Next, an SNR matrix was computed by dividing the signal magnitude matrix by the average value of a large noise region outside the phantom. To determine the image SNR improvement, profiles were selected pointing vertically through the peak SNR in each image, and the improvement was calculated as the average ratio of these profiles over the first 10 pixels, beginning with the peak. This "profile method" is illustrated in Fig. 15. Three separate trials of the above procedure were conducted; the results are summarized in Table 2.

Table 2 Planar pair SNR before and after cryo-cooling. Data was acquired with a single coil, matched and tuned with varactors at each temperature.

Data Set	Q factor RT	Q factor LT	Q Improvement factor	Expected SNR Improvement factor	Measured SNR Improvement factor
1	29.5	51.0	1.73	1.56	1.46
2	27.5	52.1	1.89	1.72	1.58
3	27.6	51.0	1.85	1.68	1.36
Avg.	28.2 ± 1.13	51.4 ± 0.63	1.82 ± 0.08	1.65 ± 0.08	1.47 ± 0.11

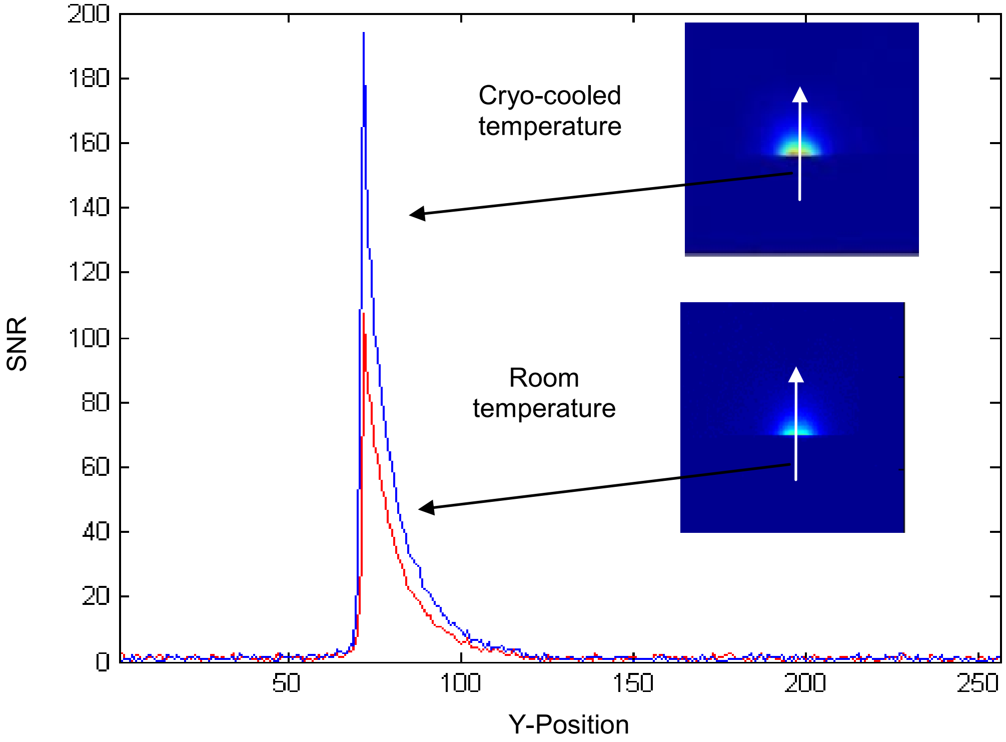

Fig. 15 SNR profiles from RT (red) and LT (blue) images (inset) as a function of y-position. The average ratio of the first 10 points beginning with the peak is used to determine the SNR improvement.

2.8 Conclusions: Planar Pairs

2.8.1 Data Analysis

Table 2 summarizes results from three experiments conducted with a single planar pair coil at RT and LT. Q measurements are also reported, and the expected SNR improvement calculated according to the following equation from subsection 2.6.4:

$$\frac{SNR_{LT}}{SNR_{RT}} = \sqrt{\frac{(Q_{LT})295}{Q_{RT}\left(\frac{(R_{coil,cold})77 + (R_{match})295}{R_{coil,cold} + R_{match}}\right)}}$$

The average predicted SNR improvement of 1.65 is quite close to the average improvement of 1.47 from imaging. Without taking the temperature of the uncooled matching network into account, the prediction would have been much higher. The ability to approximate the SNR improvement based on quick bench tests should prove a valuable tool for future cryogenic MRI projects.

In previous experiments, image SNR improvement was calculated from the peak SNR of the two images. However, it was necessary to implement the aforementioned "profile method" for evaluating the SNR improvement, due to large standard deviations observed from the simpler method. Any small movements of the coil device due to contraction upon cryo-cooling could alter the behavior of the peak SNR point. By taking an average of the ratio over the coil's region of sensitivity, these effects are averaged out.

2.8.2 Application and Improvement

While an SNR improvement of 1.47 times sounds small against the theoretical maximum of 3.3, it is still a significant achievement. This translates to a factor of two reduction in imaging time while maintaining similar SNR to an identical uncooled coil. The integration of microfluidics and a thin gas gap allow much closer proximity to the coil than would be possible with a bulky cryostat. If this SNR improvement can be extrapolated to an array of planar pair coils, it will allow higher resolution and faster SEA imaging: already one of the fastest imaging techniques.

If these goals are to be achieved, further work will be necessary in several areas. The coil-to-sample distance, while smaller than previously possible, must be reduced further still, to maximize the SNR and compete with a thin substrate uncooled coil. Coil-to-sample distance could possibly be improved with thermal insulating materials and further optimization of the microfluidic cooling channels to reduce the required volume of liquid nitrogen. In order to maximize the SNR enhancement, losses in the matching network must be minimized. Cryo-cooling the matching network would increase the SNR greatly; this would likely require the network to be integrated onto the polymer substrate with the coil. These developments could greatly enhance the sensitivity and speed of rapid imaging.

3. MICROSPIRAL COILS

3.1 Introduction

As outlined in subsection 1.6, planar microspiral coils are currently an item of interest to researchers due to their strong local sensitivity and ease of fabrication. While they do not offer SNR as high as solenoidal coils for small microfluidic samples, they work well in applications such as dermatological imaging and lab-on-a-chip systems where solenoidal microcoils are not practical.

This section will describe the work performed on spiral microcoils in our lab. Initially, we used direct coupling with varactor matching networks to couple to the microcoils, similar to those used on the planar pairs. However, direct coupling was problematic; it became clear that the convenience afforded by the varactors was not worth the cost in terms of Q factor. Thus, we began to investigate inductive coupling for microspiral coils. (One other research group has done this recently,[68, 71-74] but their work is focused on using commercial NMR probes to couple to the microspirals, and is not conducive to cryo-cooling.) While waiting for fabrication, a hand-wound coil was constructed with similar dimensions to the resonated microcoils, and tested inductive coupling to it. A simple test,[67] was used to ensure adequate coupling.

Once the resonated coils were fabricated, bench tests were executed and the design was adjusted for implementation at both room temperature (RT) and liquid nitrogen temperature (LT). Next, the coils were integrated into the microfluidic cooling device along with the secondary coils and image tests were conducted to validate predictions about SNR improvement. Finally, the results of the Q measurements and imaging tests were analyzed to reveal improvements and possible applications for the device.

3.2 Matching Network Design for Microspirals

3.2.1 Introduction: Optimizing Matching Network Design for Small Coils

Initially, plans were made to couple directly to the microspiral coils. In this case, it seemed intuitive to make the matching network as compact as possible, due to the diminutive size of the microspirals. Larger matching networks add unnecessary resistance and can distort the field pattern of the coil. Thus, a small matching network was designed to minimize the resistance and dimensions of the interconnects between the capacitors and coil. This effort also included an investigation of varactor performance to determine the relationship between biasing voltage and series resistance. In addition, a SPICE model was utilized to determine how different resistances throughout the matching network contribute to the overall noise delivered to the preamplifier. Although this work was not used in the final imaging tests, it provided enlightening information regarding the matching networks employed in the planar pairs and other MR coils.

3.2.2 Matching Network Design

The matching networks designed for the spiral microcoils were schematically the same as the network used for the planar pairs, illustrated in Fig. 10 (b). The matching network was redesigned using smaller capacitors and shrinking the overall footprint as much as possible. Two new matching networks were designed, the first with larger, high-Q hyperabrupt GaAs junction varactor diodes (MV34009, Microsemi Microwave Products, Lowell, MA), and the second with smaller, inexpensive Si varactor diodes (Infineon, München, Germany). Fig. 16 shows the two matching networks, roughly to scale.

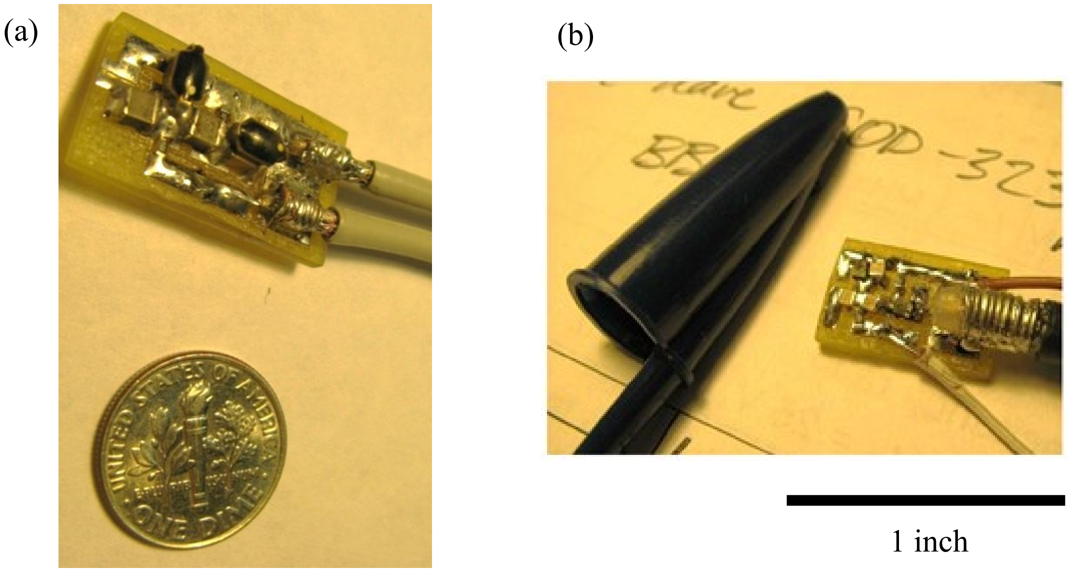

Fig. 16 Matching networks designed for direct coupling of planar microspiral coils, roughly to scale. (a) First matching network, made with B size ATC capacitors and Microsemi high-Q varactors. (b) Second matching network, made with A size ATC capacitors and Infineon. Both networks are represented schematically by Fig. 10 (b).

3.2.3 Varactor Performance

All diodes display some capacitance in reverse bias; the capacitance varies inversely to the thickness of the depletion region. Varactor diodes are a specifically designed to capitalize on this phenomenon and are used as voltage controlled variable capacitors. As the reverse bias voltage on the varactor is increased, the capacitance decreases, according to a non-linear relationship. Unfortunately, varactors have a relatively large dissipation factor (1/Q) at low biasing voltages, reducing the usable range for applications requiring high Q. Furthermore, varactor datasheets generally only specify the Q or the equivalent series resistance (ESR) at one biasing voltage and one frequency. Thus, it was necessary to gather further information to model the noise contribution of the varactors.

In order to verify the capacitance and measure the ESR of the varactors, a vector network analyzer (HP 4195A) was used along with the impedance test kit (HP 41951A), shown in Fig. 17. This system is well suited for evaluating the performance of circuit components like varactors, due to its error compensation functions, integrated DC power supply, and equivalent circuit functions.

Fig. 17 HP 41951A impedance test kit. This photograph shows a 1 inch diameter single turn coil placed in the fixture instead of a varactor diode.

In order to measure small resistances, the network analyzer must be calibrated carefully. First, precision standards were used to calibrate over a narrow frequency band (10 MHz) centered at 200 MHz. Next, the spring clip fixture was attached and a .34 cm port extension was applied to compensate for the electrical length of the fixture. Finally, an open and short compensation was completed to zero out any stray impedance.

The network analyzer was used in impedance mode, and set to display series capacitance and series resistance. This series RC model is satisfactory at VHF frequencies; any inductive reactance can be neglected. Series resistance and capacitance were approximately constant across the narrow frequency band. Hence, measurements were taken by using the network analyzer's averaging function across the entire 10 MHz span. Reverse bias voltage was increased by small intervals up to the reverse breakdown voltage specification given in the datasheets. (In the case of the inexpensive Infineon varactors, this limit was exceeded.) Fig. 18 shows the capacitance and resistance of the two types of varactors as a function of biasing voltage. It should be noted that the precision of this measurement technique is on the order of 0.1 Ω. Thus, while it is clear that the ESRs of both varactors converge to some low value, regrettably, this value cannot be measured accurately with the available equipment.

Upon initially inspecting the graphs of Fig. 18, it might be tempting to conclude that the less expensive Infineon varactors are superior. They provide more capacitance and similar series resistance to the high-Q Microsemi varactors, which cost hundreds of times more per part. This supposition is quickly debunked by examining the formula for the quality factor of a capacitor.

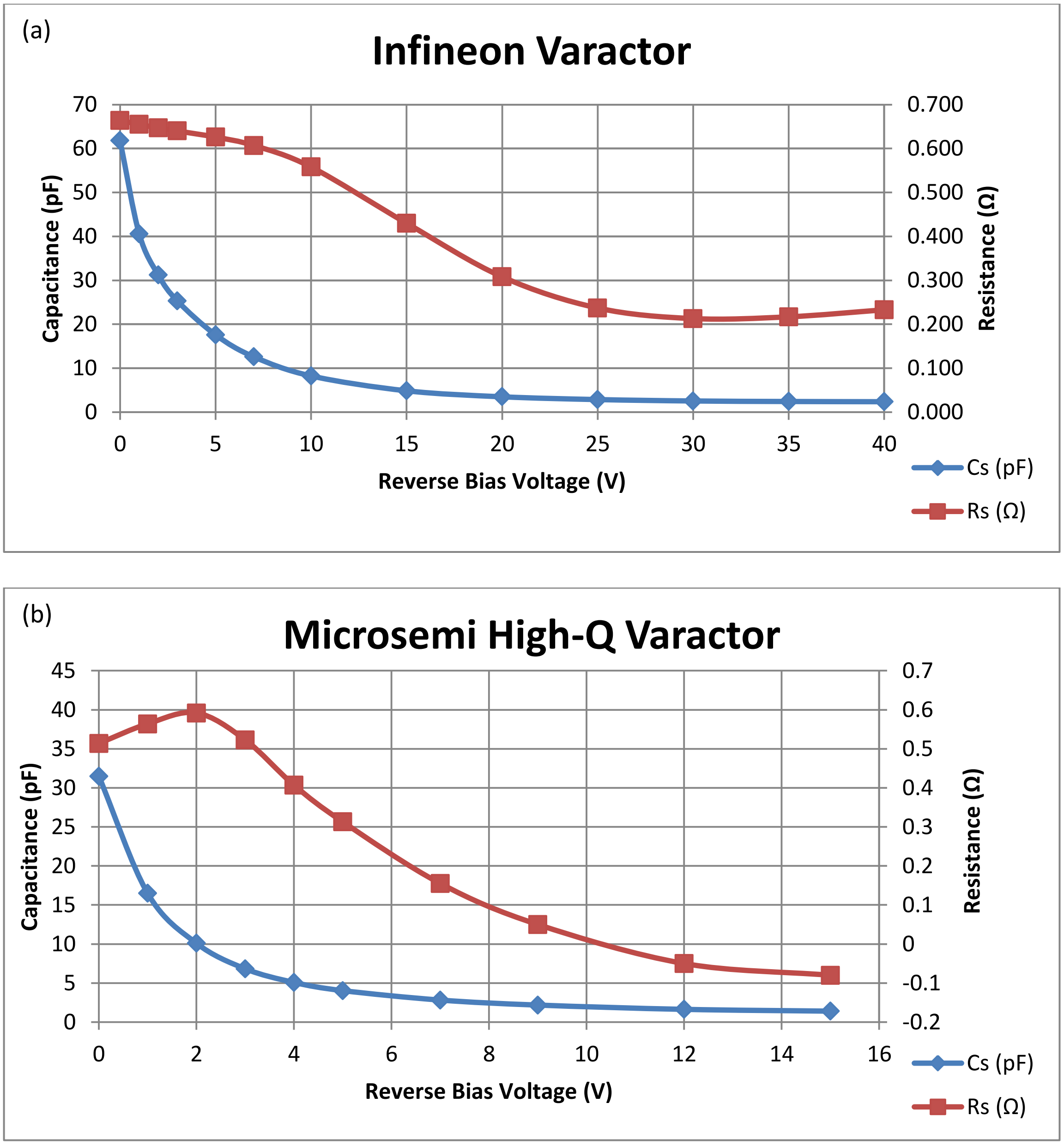

Fig. 18 Capacitance and ESR of the lower-Q Infineon varactor (a), and the high-Q Microsemi varactor (b), plotted against reverse biasing voltage. Data points are recorded in appendix B.

The quality factor (the ratio of energy stored to energy lost per cycle) is inversely proportional to the ESR, the frequency, and the capacitance, according to:

$$Q_C = \frac{1}{\omega C\ ESR}$$

Fig. 19 plots the quality factors (calculated from the above measurements) versus reverse biasing voltage for the two different varactors. Clearly, the Q of the Microsemi diode is far superior to that of the Infineon. In addition, the lesser expensive Infineon requires operation at much higher DC voltages, requiring less readily available DC power supplies, and introducing a potential shock hazard.

This information is extremely valuable for matching network design, in a number of ways. Knowledge of these relationships informs the designer of what voltage will be optimal for matching and tuning, in order to minimize the loss in the capacitor. In addition, this will greatly speed the process of finding the proper biasing capacitors.

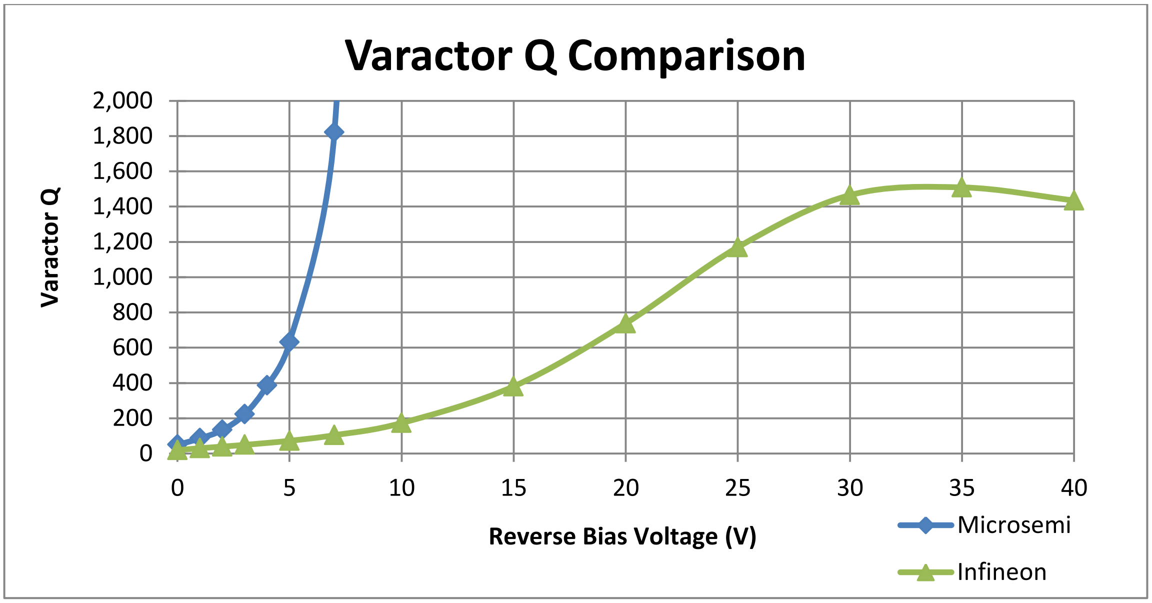

Fig. 19 Comparison of varactor Q factors as a function of reverse bias voltage. The graph is not scaled higher than Q = 2000 because the Microsemi high-Q varactor resistance became too small to measure accurately with the available equipment. Measurements were conducted at 200 MHz. The data is recorded in appendix B.

3.2.4 Noise throughout the Matching Network

Even after gaining a good understanding of the loss in a varactor, there was still the question of how that resistance specifically affects the SNR of the imaging experiment. A SPICE simulation was used to model the coil and matching network. Inductance and capacitance values were chosen to resonate at 200 MHz with a Q of 30. In addition to the idealistic components, a small resistance and a voltage generator was added in series with each capacitor to model the ESR and thermal noise of a varactor. A voltage generator was also added in series with the coil to simulate an NMR signal. (See Fig. 20) To determine the effect of noise generated at each varactor, a frequency response simulation was run three times, once with each source turned on individually to 1 V AC. Signal was probed at the 50 Ω load (representing the preamplifier).

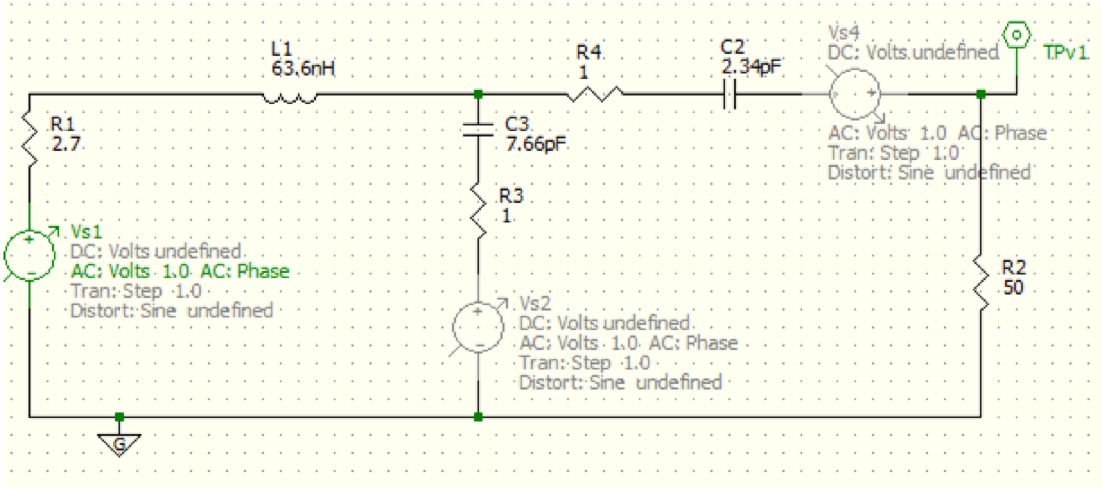

Fig. 20 SPICE model of coil and matching network. Each voltage source was turned on individually and the output at the 50 Ω load was measured.

All three simulations results peaked at 200 MHz. The coil voltage source, representing an NMR signal, delivered 5.7 dB to the load. The tune varactor voltage source delivered 3.4 dB, but the match varactor voltage source delivered only -7 dB to the load. While not a rigorous noise evaluation, this makes it clear that the most important design considerations here are the reduction of coil resistance, ESR of the tune capacitor, and resistance of the connections between them. Thermal noise after the tune capacitor will have a much smaller effect.

3.3 Bench Test of Directly Coupled Microspiral Q Factors

Chiwan Koo's first batches of microfabricated microspiral coils had both 2-turn and 3-turn coils on the substrate. All coils fabricated had a 2 mm inner diameter, 40 μm trace width, and 30 μm trace separation. The trace thickness varied slightly batch to batch, but generally, the target thickness was 25 μm. This design closely resembles the coil design of Massin, *et al.*[47] Early batches were fabricated with 40 μm copper traces running away from the coil to solder pads for soldering to a matching network. Unfortunately, the working coil yield was generally quite low. Thus, working coils were identified by testing for continuity and resistance with an ohmmeter. Next, impedance was measured with a vector network analyzer (HP 4195A) to determine effective inductance at the operating frequency of 200 MHz. In this way, proper operation of coils was verified before the coils were matched and tuned. The 2-turn coils had an inductance of 20 nH and the 3-turn coils had an inductance of 42 nH, using the approximations of Mohan, *et al.*,[40] and observed inductances were similar to the approximations.

Next, a working 3-turn coil was coupled to a 50 Ω coaxial transmission line with the matching network from Fig. 16 (a). PDMS microfluidic cooling channels were affixed to the coil substrate, and the Q was measured at RT and LT. In three trials, the Q increased by a factor of 1.8 on average. In addition, in several trials, the matching network was partially cooled by directing the exit flow of liquid nitrogen towards the matching network board. This resulted in a further increase in the Q factor, up to 2.4 times the Q at RT. This suggests that a significant amount of resistance is contributed by the matching network. Q measurements of these directly coupled spiral microcoils are shown in Table 3. In a separate trial, a 3-turn microspiral capacitor was tuned and matched with Voltronics capacitors. At RT, the Q was 36.6, increasing by a factor of 1.8 after cryo-cooling. Thus, even high-Q varactors can degrade Q quite significantly.

Table 3 Q factor of a directly coupled 3-turn microspiral coil. High-Q varactors were used to match and tune. The Q increased dramatically when the matching network was cooled as well.

Data Set	RT Q	LT Q	LT Q + Matching network cooled
1	26.8	47.1	—
2	26.4	47.5	63.5
3	27.0	46.5	65
Average	**26.7**	**47.0**	**64.3**

3.4 Investigating Inductive Coupling

3.4.1 Inductive Coupling and Microcoils

Just as an NMR signal can be coupled inductively to a coil, a signal in one coil can be coupled inductively to another coil. As discussed in subsection 1.8, it is possible to place a surface coil in close proximity to the sample being imaged, and then detect this signal with a secondary coil. The secondary coil is then coupled directly to a transmission line. This translates to an enormous amount of flexibility with regard to coil placement. For example, inductive coupling has been utilized to design implantable probes that can be coupled to from outside an animal's body.[66]

Inductive coupling has only recently been applied to microcoils.[68-74] However, there are multiple reasons for pursuing inductive coupling for cryo-cooled microspirals. First, it circumvents the difficulty of connecting a matching network to such a small coil. In addition, by eliminating connection wires, heat flux to the coil is reduced, requiring less liquid nitrogen for adequate cooling. Thus, it was decided to pursue the fabrication of a microspiral coil with an integrated microfabricated capacitor. The 3-turn spiral microcoil design itself was not changed, but a parallel plate capacitor with an SU-8 dielectric layer was added to resonate the coil.

3.4.2 Ensuring Adequate Coupling

One great advantage of inductive coupling is that the primary coil is not tethered to a direct wire connection, which would hinder the freedom of coil placement. There is inevitably some degradation in SNR when using inductive coupling compared to what could be achieved through direct coupling (assuming no matching network losses). However, if the level of coupling between the primary and secondary coils is high enough, this SNR degradation is small and can be neglected. Steven Wright explored this in a conference proceeding and developed an easy method of determining if adequate coupling is achieved.[67] As Wright points out, it is difficult to directly calculate or measure the mutual inductance or coupling coefficient between two coils. The level of coupling varies with coil geometry and relative placement. However, a straightforward indicator of coupling is the change in input resistance of the secondary coil.

In this method, the input resistance of the isolated secondary coil is measured first. Then, the input resistance is measured again with the secondary coil coupled inductively to the resonated primary coil. Ideally, the input resistance should rise by a factor of 10 or greater at the resonant frequency; this will result in an SNR that is only degraded 5% from the case of ideal direct coupling. Coupling can be increased by bringing the coils closer together or changing the design of the coils.

3.4.3 Testing with Hand-Wound Coil

While waiting on coil fabrication, and to determine the feasibility of coupling to spiral microcoils, a small hand-wound coil was constructed out of insulated 30 gauge wire. (See Fig. 21)

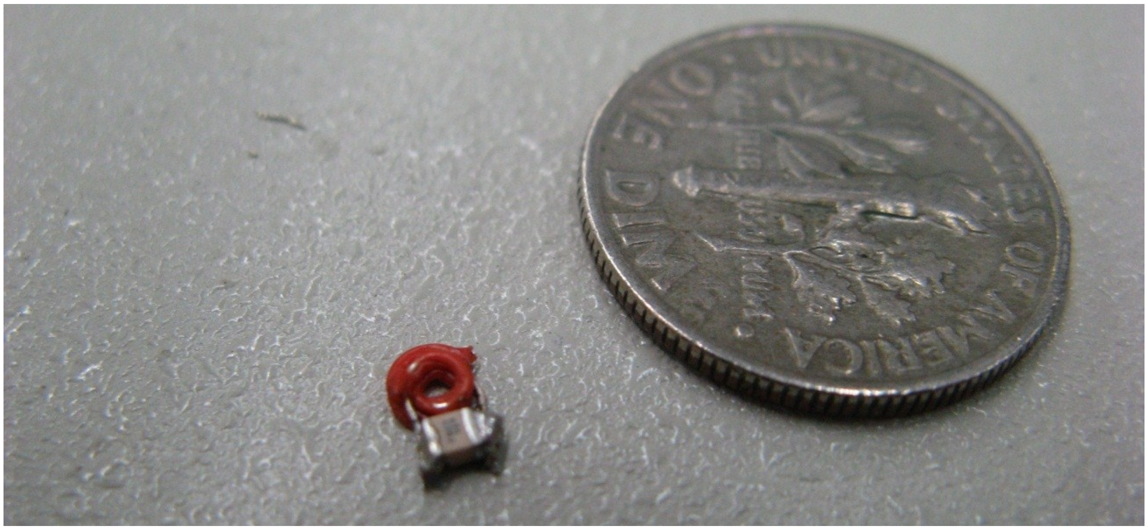

Fig. 21 Hand-wound coil resonated with ceramic capacitor.

The coil was made with 3 turns and an inner diameter of approximately 2 mm to make it as similar to the microcoils as possible. A small 43 pF ceramic capacitor was used to resonate the coil at 200.1 MHz. (Note that the inductance is around 15 nH, significantly lower than the spiral microcoils.) The Q of the hand-wound coil was measured with dual flux probes, giving Q = 90.

Next, a 1 cm diameter secondary coil was hand made with 3 turns of 18 gauge magnet wire (Fig. 22). This coil has an estimated high-frequency resistance of 0.3 Ω at 200 MHz, including proximity effects and the skin effect. According to theory and measurements, its inductance was around 100 nH.

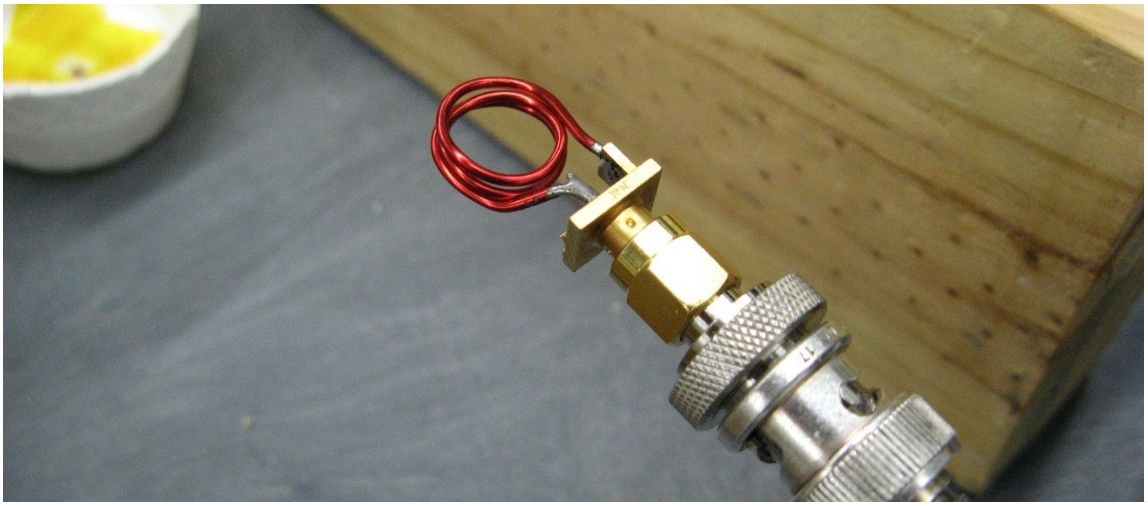

Fig. 22 Secondary coil used for inductive coupling experiments.

The best tool available for measuring impedance at 200 MHz was an HP 4195A Vector Network Analyzer/Impedance Analyzer. This instrument converts an S_{11}

measurement into an impedance measurement. Thus, the accuracy is generally acceptable in a range from 1 Ω to 10,000 Ω. Thus, it was not possible to measure very small resistances (such as the input resistance of this uncoupled secondary coil), with accuracy. However, after calculating the resistance from the geometry of the coil, the desired input resistance was 3 Ω or greater after coupling to prevent degraded SNR. Three ohms is measurable with acceptable accuracy, and this degree of coupling was easily achieved by aligning the hand-wound coil with the secondary coil, separated by 1 cm or less. This was a reassurance that adequate coupling could be achieved with coils of this geometry.

3.4.4 Testing Microfabricated Microspirals

After fabrication of the microcoils with integrated capacitors, the microcoils were tested for their resonant frequency with the network analyzer and the secondary coil described previously. The capacitors in the first few batches had capacitances that were too small, resulting in a resonant frequency above 200 MHz, and there was no way to lower this resonance. Later batches were fabricated with a thinner SU-8 layer to increase the capacitance. Once a coil was obtained which had a resonant frequency below 200 MHz, small areas of the capacitor were removed with an X-Acto knife under a microscope until the resonant frequency was raised to 200.1 MHz. Measuring the quality factor with dual flux probes, the coils were determined to have a Q of approximately 12 at room temperature. (Much lower than expected, based on direct coupling to similar coils (subsection 3.3)).

3.4.5 Effects of Cryo-Cooling on Microfabricated Spiral Microcoils

Once a microcoil was successfully resonated at 200.1 MHz (at RT), it was immersed in liquid nitrogen. Strangely, the resonant frequency of the coil rose by 12% after cryo-cooling. Initially, this was attributed to thermal shrinkage due to the extreme change in temperature. However, after closer examination, the shrinkage of the copper coil was shown to be insignificant in this regard. Thus, the resonance shift was attributed to a decrease in the permittivity of SU-8 after cryo-cooling. Detailed data about the frequency and temperature dependence of SU-8's permittivity were not found.

After cryo-cooling, the Q of the microfabricated coils (measured with dual flux probes) was consistently around 70. This is approximately a 6-fold improvement over the room temperature quality factor, much higher than the factor of 2.8 predicted as the maximum attainable with coil dimensions larger than the skin depth (see subsection 2.6.3). Due to the low Q at room temperature and the large shift in resonant frequency after cryo-cooling, it was necessary to investigate the dielectric properties of the SU-8 dielectric material.

3.4.6 Characterization of SU-8 Dielectric

Thus, on a subsequently fabricated substrate, an isolated parallel plate capacitor with SU-8 dielectric was fabricated without an accompanying coil. The parallel plates had dimensions 3 mm by 4 mm with a 14.8 µm thick SU-8 dielectric layer. The network analyzer (HP 4195A) was calibrated with a semi-rigid coaxial probe, using a port extension and compensation. This probe was then soldered to the microfabricated capacitor (see Fig. 23) and the impedance was measured at 200 MHz. At room temperature, the capacitor had a capacitance of 31 pF with a series resistance of 1.5 Ω. After cryo-cooling, the capacitor had a capacitance of 24 pF and negligible series resistance. This corroborates the microfabricated coil Q measurement data. When directly coupled, the coils had a Q around 40. Assuming an inductance of 42 nH, this translates to a room temperature coil resistance of approximately 1.3 Ω. To resonate this around 200 MHz requires a 15 pf capacitor, half the size of the measured capacitor. A capacitor of half the area will have half the capacitance, but double the series resistance. Thus, the capacitor used to resonate the coil has approximately 3 Ω ESR. Adding this to the coil resistance gives 4.3 Ω total resistance and a Q of 12, consistent with the Q measurements. In addition, the 22% decrease in capacitance measured after cryo-cooling corresponds approximately to the observed 12% increase in resonant frequency according to the LC resonance equation:

$$\omega = \frac{1}{\sqrt{LC}}$$

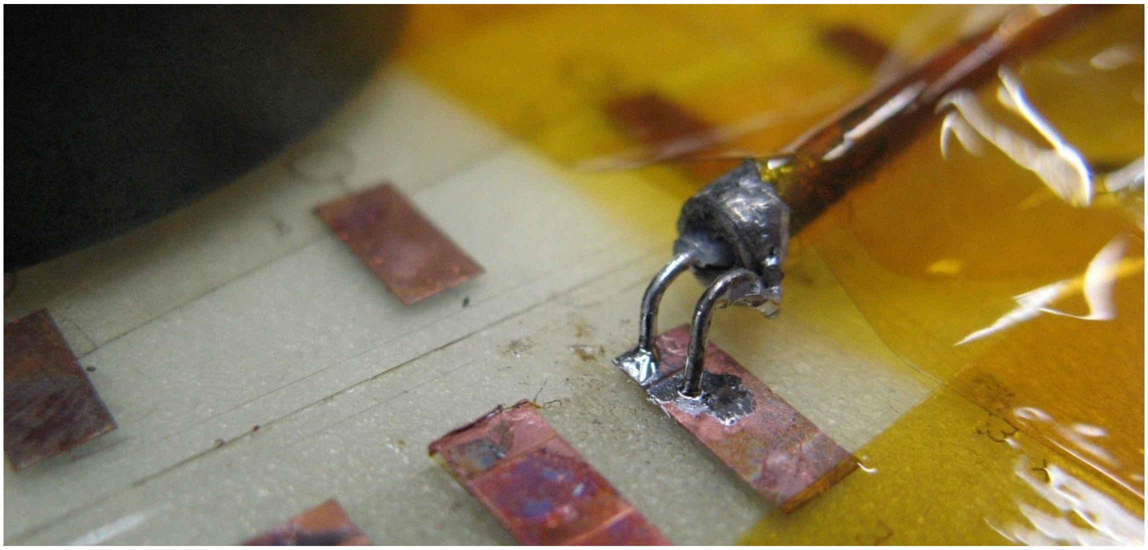

Fig. 23 Microfabricated parallel plate capacitor for determining SU-8 dielectric properties at 200 MHz. The parallel plates had dimensions 3 x 4 mm and the SU-8 thickness was 14.8 µm.

Based on these measurements, the relative permittivity of SU-8 at 200 MHz can be estimated to be 4.3 at room temperature and 3.4 at 77 K.

3.5 Bench Testing with Inductive Coupling

3.5.1 Measuring Input Resistance

As shown in subsection 3.4.2, the input resistance of the secondary coil should increase by a factor of 10 when coupled to the primary coil, in order to maintain 95 % of the available SNR. The secondary coil, described in subsection 3.4.3, has a self-resistance of 0.3 Ω. Thus, an input resistance measurement of 3 Ω or greater is desired when the coil is coupled. To test this, a coil substrate with two microfabricated coils (one tuned for RT, the other tuned for LT) was coated with 7 mm deep PDMS. A cryo-cooling channel was added over the LT coil. First, the probe shown in Fig. 22 was affixed over the RT coil with tape and the input resistance was measured. The input resistance rose only minimally, from 0.3 Ω to approximately 0.5 Ω. This measurement was not very precise; reflection-type impedance measurements are not preferred for impedances below 1 Ω. Clearly, though, the coupling is not optimal at room temperature.

Next, the probe was affixed over the LT coil and the coil was cryo-cooled. In this case, the input resistance rose to 2 Ω. This is on the order of the level of coupling that was desired, but not quite optimal. Thus, in the final design, the secondary coils were embedded in the polymer coating, reducing the separation to approximately 4 mm. Since the secondary coils were already affixed to the matching networks, it was not possible to measure the coupled input resistance directly. However, the coupling increases rapidly as the coils are brought closer, and the LT coil coupling was certainly well above the 3 Ω benchmark.

3.5.2 Secondary Coil Matching Network

Initially, the matching network was designed with varactors. However, it became apparent that varactors were not suitable for transmit-receive imaging, because the level of power required for transmit would detune the varactor circuit. (Transmit-receive imaging was used to avoid coupling issues with the volume coil.) Thus, 1 pF – 5 pF variable capacitors were used on the matching network. An added advantage of using these capacitors was that a much higher Q was obtained than was achieved with varactors. However, these capacitors must be adjusted manually, outside the magnet bore. Fig. 24 shows one of the secondary coils and matching networks.

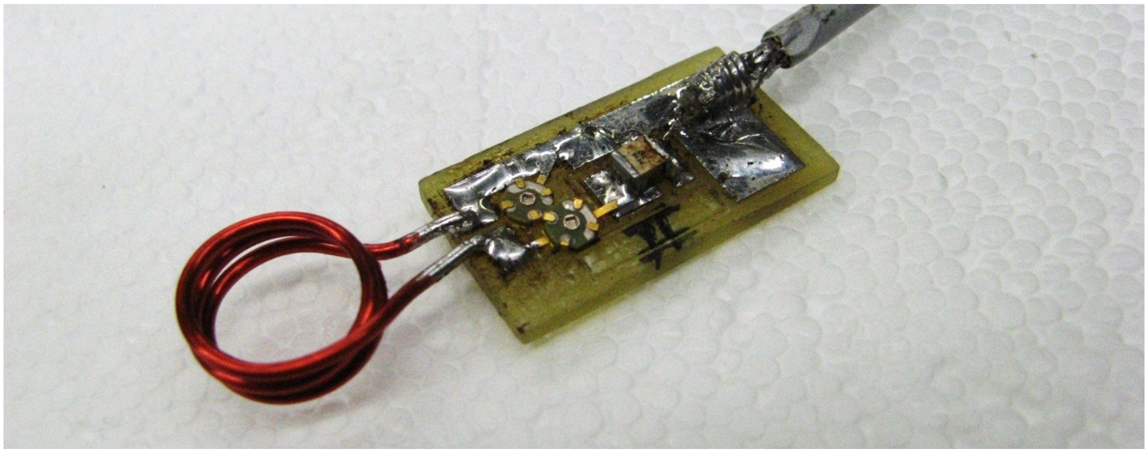

Fig. 24 Secondary coil and matching network. Coil is 1 cm in diameter.

3.5.3 Q Measurements

As stated previously, the Q of the microfabricated coils at RT was measured to be consistently around 12 Ω, using dual flux probes. After cryo-cooling, this Q increased 70. The secondary coils were tuned and matched with the matching network described in subsection 3.5.2 and the uncoupled Q was measured to be approximately 200, using the 7 dB return loss method.

Next, the secondary coils were embedded into the polymer coating over the primary coil substrate. Fig. 25 shows the substrate, secondary coils, and microfluidic cooling channel. After integrating the primary and secondary coils, reflection-type Q measurements were no longer possible. When coupled, the frequency response changes and the assumptions in subsection 2.2 about return loss are no longer valid. However, we can use the prior Q measurements to predict the SNR advantage of the LT coil over the RT coil.

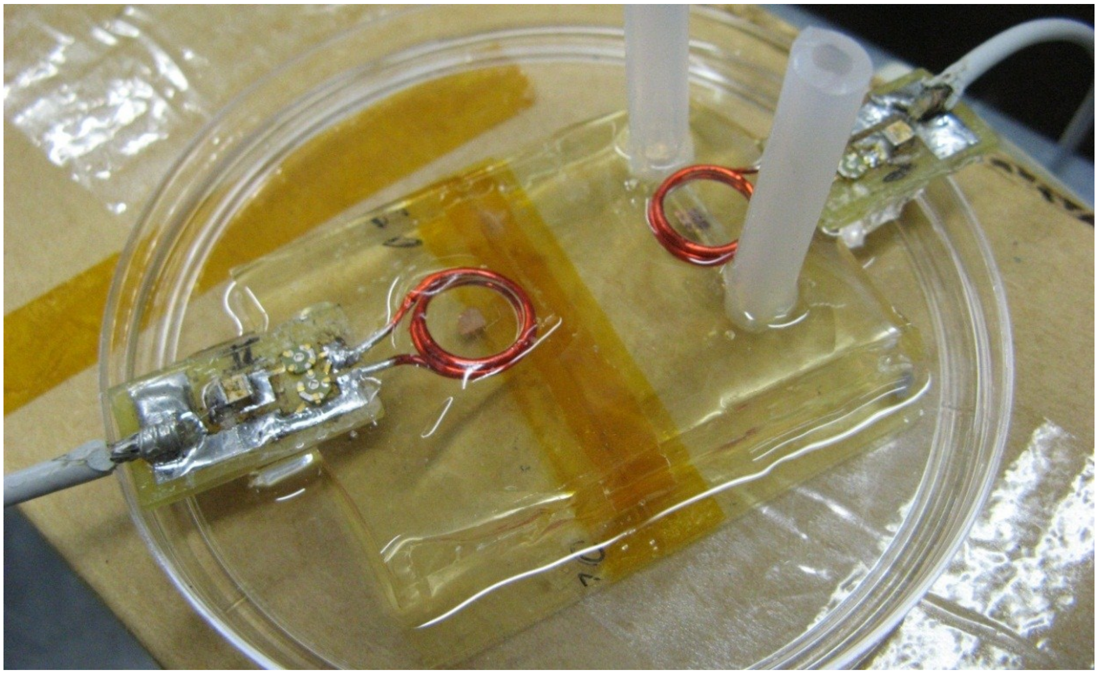

Fig. 25 Substrate with primary coils, covered with PDMS coating. Secondary coils are embedded in the PDMS, approximately 4 mm above the substrate.

3.6 Imaging with Microspirals

3.6.1 First Attempt

The first microspiral imaging attempt was only with an RT coil. The secondary coil was separated from the coil substrate by a 7 mm thick piece of PDMS, and the substrate was taped to a phantom. A wave trap balun was connected in line with the signal cable to prevent losses due to shield currents. The coil assembly and balun were affixed to the acrylic sled used for planar pair imaging and inserted into the bore of the magnet. Matching and tuning the secondary coil was done outside of the bore, and then the return loss was verified after insertion.

In the bench test, the secondary coil input resistance rose minimally when spaced 7 mm from the microcoil. Not surprisingly, the image results showed little coupling as well. Gradient echo and spin echo pulse sequences were used with coronal (in the plane of the coil substrate) and transverse (perpendicular to the bore of the magnet) slices in an attempt to find the sensitivity pattern of the microcoil. Instead, the pattern was large and dispersed, reflecting only the sensitivity of the secondary coil alone. Fig. 26 shows a coronal slice acquired with a spin echo sequence and a transverse slice acquired with a gradient echo sequence. Note that gradient echo is a very fast sequence, useful for finding slices quickly. However, it is prone to susceptibility artifacts; spin echo generally produces cleaner images.

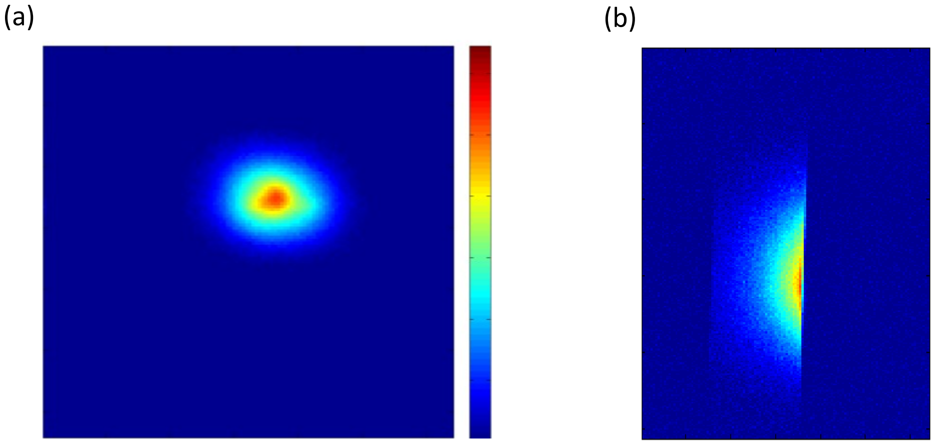

Fig. 26 Images acquired with RT coil separated by 7 mm from secondary coil. (a) Spin echo coronal image, 50 x 50 mm field of view. (b) Gradient echo transverse image, 50 x 30 mm field of view.

3.6.2 Hand-Wound Coil

Next, the hand-wound coil described in subsection 3.4.3 was placed on the phantom and separated from the secondary coil by a 7 mm piece of PDMS. Bench testing of the hand-wound coil showed adequate coupling for coil-to-coil distances less than 1 mm. Images were acquired, and the difference in pattern was distinctly noticeable from the first RT microcoil test. Fig. 27 shows two images acquired with hand-wound coil, with power calibrated for maximum signal.

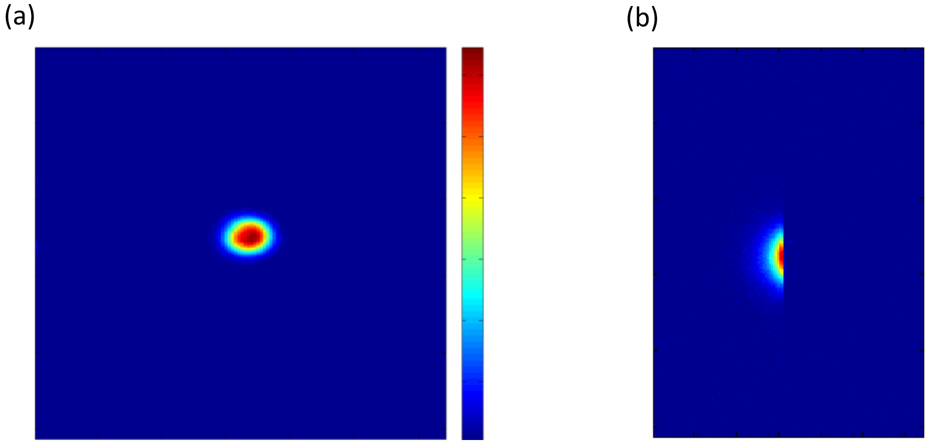

Fig. 27 Images acquired with hand-wound coil. (a) Spin echo coronal slice, approximately 90° 180° flip angle, 50 x 50 field of view. (b) Gradient echo transverse slice, approximately 90° flip angle, 50 x 30 field of view.

3.6.3 First Cryo-Cooling Test

After the results of the first test, where the RT coil had almost no visible coupling, the cryo-cooling device was designed to place the secondary coil only 4 mm away from the primary coil. This device, shown in Fig. 25, was used for the next three imaging tests. The closer proximity of the coils appeared to increase the coupling greatly, even at RT. Fig. 28 shows spin echo coronal slices at RT and LT. The peak SNR ratio of LT to RT was 4.9 in this test, determined from the coronal slices. Ice formation caused the coil to detune before LT transverse slices could be acquired.

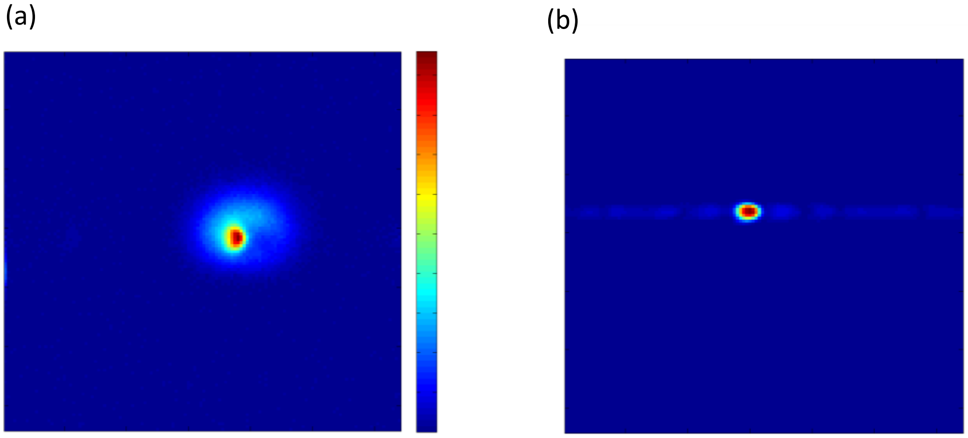

Fig. 28 First test, coronal spin echo images, acquired with RT and LT microcoils. 50 x 50 mm field of view, approximately 90° 180° flip angles. (a) LT (b) RT.

3.6.4 *Second Cryo-Cooling Test*

After the first test with the RT and LT microcoils, the device was removed from the magnet and allowed to dry for several days. The second test was carried out with the same methodology as the first test. Both coronal and transverse slices were acquired at RT and LT. Fig. 29 shows the transverse images. The coronal SNR ratio was 3.64 in this experiment, and the transverse SNR ratio was 3.99.

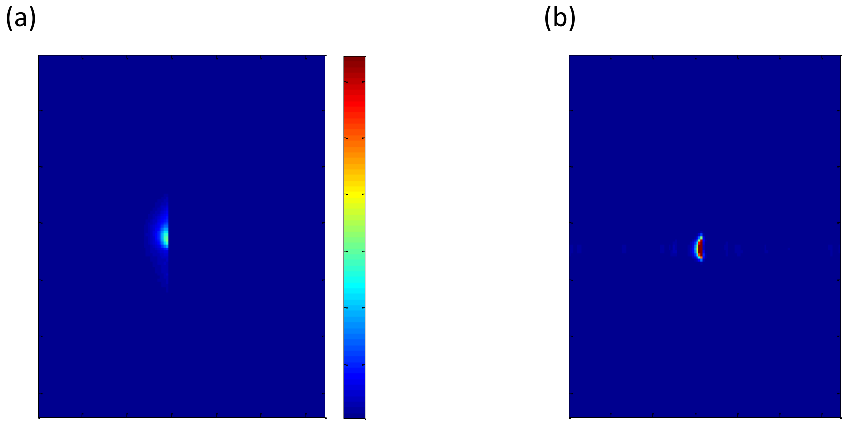

Fig. 29 Second test, transverse spin echo images, acquired with RT and LT microcoils. 50 x 30 mm field of view, approximately 90° 180° flip angles. (a) RT (b) LT.

3.6.5 Third Cryo-Cooling Test

A third cryo-cooling test was attempted and RT images were acquired, but the LT coil became detuned possibly due to ice formation. Currently, it is not clear whether the coil is damaged or still in working order for an additional test.

3.7 Conclusions: Microspirals

3.7.1 Predictions and Results

Based on the Q measurements of the microspirals, the SNR enhancement due to cryo-cooling can be predicted, using the equations from subsection 2.6.2:

$$\mathrm{SNR}_{\mathrm{improvement}} = \sqrt{\frac{\mathrm{T}_{\mathrm{room}}/\mathrm{Q}_{\mathrm{room}}}{\mathrm{T}_{\mathrm{cooled}}/\mathrm{Q}_{\mathrm{cooled}}}} = \sqrt{\left(\frac{295}{77}\right)6} = 4.8$$

This estimate assumes that both microcoils were well coupled to the secondary coils and had negligible sample loading. The data collected supports these assumptions. The data from the first two experiments, while limited, seems to support this estimate of SNR enhancement. The second experiment also showed an encouraging increase in the SNR due to cryo-cooling, but highlighted a lack of precision in the power calibration and slice selection at room temperature. This can be solved by using a consistent slice selection methodology, which was going to be implemented in the third experiment.

3.7.2 Possible Future Improvements

Although the Q and SNR enhancement observed in the inductively coupled microspirals was quite impressive, the comparison was somewhat skewed due to the large dielectric losses at room temperature. For a more realistic comparison, the coils should be designed with higher-quality capacitors that have negligible loss as room or cryo-cooled temperatures. In this case, the maximum SNR improvement that could be attained with copper coils would be 3.3, as discussed in subsection 2.6.4. In this investigation, redesigning the capacitors with a superior dielectric material was not feasible, but the SU-8 dielectric served well as a proof of concept. It would have been preferable in this study to have a dielectric material with properties that did not vary significantly with temperature. However, this would not be an important consideration for an end application, where the coil would always be used at liquid nitrogen temperature. Similarly, SU-8 could continue to be used for cryo-cooled applications if it can be verified that the loss is truly negligible at liquid nitrogen temperature.

In addition to finding a better dielectric material, the design of the capacitors needs improvement. It was very difficult to adjust the resonance of the coils accurately in this study. The capacitors should be designed with perforations or fingers to allow small portions of capacitance to be removed quickly and accurately. If the microfabrication process is perfected and high-precision machinery is available, it may be possible to fabricate capacitors that do not need adjustment to resonate the coil at the correct frequency.

To obtain greater SNR enhancement and make cryo-cooled spiral microcoils more competitive with other techniques, high temperature superconductor (HTS) coils should be considered. Because HTS coils would require only liquid nitrogen cooling, the cryogenics would not be any more complicated than cryo-cooling copper coils as demonstrated here. The issues of HTS coil fabrication and integration with a high-Q capacitor would need to be addressed. An HTS coil will generate no thermal noise in the coil itself. Thus, the SNR would be limited instead by the noises generated in the capacitor, sample, secondary coil, and transmission line, as well as the noise figure of the preamplifier. This could be optimized to generate a tremendous SNR enhancement for microscopy.

In our coils, the samples were placed outside of the optimal imaging range. Realistically, the decreased sensitivity due to this spacing outweighs the benefits of increased sensitivity due to cryo-cooling. If the microfluidics can be improved by minimizing channel volume, a smaller quantity of liquid nitrogen will be required to cryo-cool the coil. This would allow for closer coil-to-sample placement, making cryo-cooling a viable option for SNR enhancement.

3.7.3 Microspiral Applications

Cryo-cooling of copper coils offers a potential 2.8 times increase in SNR, if coil-to-sample distance is not increased significantly. This could allow a reduction of acquisition time by a factor of eight, an increase in isotropic imaging resolution by a factor of 1.4, or a combination of increased resolution and shortened imaging time. (Spectroscopy resolution could be increased by 2.8.) Potentially, even greater gains could be made with HTS microspiral coils. These increases make the microspiral geometry an attractive competitor against solenoidal microcoils for mass-limited spectroscopy detection. Because of its planar geometry, the microspiral can be more easily produced and integrated into lab-on-a-chip applications for spectroscopy and imaging.

Another application of inductively coupled microspirals would be an embedded coil. Cryo-cooling of the primary coil could not be used for an embedded coil, but the SNR gains due to extremely close proximity would help balance this out. A one-time procedure could embed the coil, allowing future non-invasive close inspection of a specific internal tissue, with a secondary coupling coil outside the body. Embedded coils have been demonstrated before,[66] but not with microspiral coils.

For skin microscopy or other external imaging, a cryo-cooled microspiral with a thin nitrogen gas gap could be employed for rapid imaging and diagnosis. The concept of an array of microcoils (discussed in the following subsection) would allow surface microscopy of a wider field of view. Cell counting and identification are other possible applications of spiral microcoils.

3.7.4 Extension to an Array of Microspirals

Wright demonstrated spine imaging with an array of mutually coupled surface coils.[61] Multiple primary coils are used and coupled to a single secondary coil, allowing a wider field of view with the high SNR of a surface coil. This concept can be extended to an array of microspiral coils, allowing wide field of view surface microscopy. Cryo-cooling can easily be extended to an array with microfluidic channels over all the coils.

Because the microcoils each have a very narrow field of view, they would need to be placed very closely together. Thus, the capacitor size would need to be decreased. This could most readily be achieved by decreasing the thickness of the dielectric layer in the capacitors or using a dielectric material with a higher permittivity. Otherwise, the capacitors could be redesigned with an interdigitated finger design or small ceramic capacitors could be soldered to the coils. For this application, it would be extremely helpful to have an accurate enough fabrication process to eliminate the need to hand-tune each coil.

4. SUMMARY AND CONCLUSIONS

4.1 Summary

4.1.1 Planar Pairs

This study is the culmination of work on a grant, which sought to apply cryo-cooling to copper coils of smaller geometries than had been cryo-cooled previously. First, cryogenics were integrated with planar pair coils, a coil design used by our research group for a rapid imaging technique known as Single Echo Acquisition (SEA) imaging. The work with planar pairs and the need for accurate Q measurements to correlate to our image SNR data prompted us to develop an accurate method of reflection-type Q measurements, referred to as the "7 dB method." To better understand the loss mechanisms which reduce the Q and image SNR of the planar pairs, the performance of the varactors used in the matching network were characterized and the effects of noise in the matching network were modeled. After extensive bench testing at room and cryo-cooled temperatures, imaging tests were conducted with the planar pairs and observed an average SNR gain of 50%. Afterwards, the disparity between this improvement and the theoretical maximum was analyzed, revealing future improvements that will allow greater gains in SNR. Results of this planar pair work were published in a journal paper.[80] Work is continuing to apply cryogenics to an array of planar pairs, to increase the SNR of SEA imaging, with the main obstacle being the tendency to lower the image surface temperature below freezing.

4.1.2 Microspiral Coils

Microspiral coils, similar in design to those of Massin, *et al.*,[47] were microfabricated by Chiwan Koo. Initially, the coils were bench tested with direct coupling using varactor matching networks similar to the ones used for the planar pairs. However, due to the small geometry of the microspirals and the importance of thermal isolation, inductive coupling was investigated. A hand-wound microcoil was fabricated to investigate the feasibility of inductive coupling to the microspirals, yielding positive results.

Microfabricated parallel plate capacitors were added to resonate the planar microspiral coils. It was necessary to fabricate separate coils for room temperature and cryo-cooled temperature imaging, due to a resonance shift after cryo-cooling. This shift, along with the inexplicably low Q of the coils at room temperature prompted an investigation into the permittivity and losses in the dielectric material used in the capacitors. Bench tests were then conducted on the RT and LT microcoils to confirm resonant frequency, Q, and adequate coupling to the secondary coil. Finally, images in three separate trials were acquired with the RT and LT coils to determine the SNR improvement due to cryo-cooling.

An average SNR increase of four times was observed in the imaging tests. This sensational result is tempered by the reality that the SU-8 dielectric layer was lossy at room temperature, causing a larger Q and SNR increase after cryo-cooling. The results of imaging and bench tests were analyzed, showing good agreement between theory and results. Possible improvements and applications for the coil and capacitor design were identified to guide future work. A journal paper is being prepared to report the results of this research, focusing on the mutually beneficial unification of two techniques: inductive coupling and cryo-cooling for maximum sensitivity.

4.2 Conclusions

4.2.1 Planar Pairs

This study demonstrates that the SNR of planar pair coils can be improved through cryo-cooling. Further work will be necessary to develop cryo-cooled planar pairs into a useful imaging method. Most importantly, since planar pairs are used in arrays, the cryo-cooling technique must be improved to cryo-cool an entire array of planar pairs (generally 64 channels) without lowering the imaging surface temperature below freezing. In addition, planar pairs have a very limited imaging depth, approximately equal to the width of the planar pair coil. Thus, the coil-to-sample distance must be kept as small as possible. Realistically, the 50% increase in SNR gained in this study is likely negated by the increased coil-to-sample distance, due to the necessity of a gas-phase N_2 gap. Thus, to make this concept valuable, the SNR enhancement must be optimized by using high-Q matching network components (and possibly cryo-cooling the matching network) while minimizing the coil-to-sample distance. If this balance can be maintained, cryo-cooling could prove invaluable for increasing the SNR of SEA imaging experiments, one of the fastest MR imaging techniques, allowing high quality images at frame rates approaching 1000 Hz.

4.2.2 Microspiral Coils

A significant increase in SNR due to cryo-cooling of inductively coupled microspiral coils has been demonstrated. This was achieved through the use of a high-Q secondary coil and matching network. Some aspects will need to be improved to make this a convenient design. The microfabricated capacitor should be made with a superior dielectric material and designed for convenient resonance adjustment. Even with these caveats, the image SNR improvement is quite impressive and promising for use in microscopy and spectroscopy applications.

Microcoils face the same restriction as planar pairs regarding imaging depth. Since the useful imaging depth is approximately equal to the diameter of the coil, magnetic resonance experiments employing cryo-cooled microspirals will be limited to larger diameter (> 1 mm) coils for the time being. However, it is possible that creative methods will reduce the coil-to-sample distance, allowing even smaller microcoils, for higher resolution imaging and spectroscopy of mass-limited samples.

Inductive coupling adds another difficulty: the requirement of adequate coupling between the primary and secondary coil. Fortunately, it has been shown that this requirement can be easily satisfied with these coils and verification is not difficult. Furthermore, the benefits in terms of thermal isolation and freedom of coil placement are more than worth the efforts required.

Finally, a promising future application of microspiral coils is an inductively coupled, cryo-cooled array of microspiral coils. This array would allow fast, high-resolution, wide field-of-view microscopy for dermatological imaging and other similar applications.

REFERENCES

1 W. Gerlach and O. Stern, *Z. Phys. A*, 1922, **9**, 353-355.

2 I. I. Rabi, J. R. Zacharias, S. Millman and P. Kusch, *Phys. Rev.*, 1938, **53**, 318.

3 F. Bloch, *Phys. Rev.*, 1946, **70**, 460-474.

4 P. C. Lauterbur, *Nature*, 1973, **242**, 190-191.

5 P. Mansfield, *J. Phys. C: Solid State Phys.*, 1977, **10**, L55-L58.

6 P. Mansfield and A. A. Maudsley, *Br. J. Radiol.*, 1977, **50**, 188-194.

7 M. K. Stehling, R. Turner and P. Mansfield, *Science*, 1991, **254**, 43-50.

8 Z.-H. Cho, J. P. Jones and M. Singh, *Foundations of Medical Imaging*, John Wiley & Sons, Inc., New York, 1993.

9 Z.-P. Liang and P. C. Lauterbur, *Principles of Magnetic Resonance Imaging: A Signal Processing Perspective*, IEEE Press, New York, 2000.

10 P. B. Roemer, W. A. Edelstein, C. E. Hayes, S. P. Souza and O. M. Mueller, *Magn. Reson. Med.*, 1990, **16**, 192-225.

11 D. I. Hoult and P. C. Lauterbur, *J. Magn. Reson.*, 1979, **34**, 425-433.

12 W. A. Edelstein, G. H. Glover, C. J. Hardy and R. W. Redington, *Magn. Reson. Med.*, 1986, **3**, 604-618.

13 D. I. Hoult and R. E. Richards, *J. Magn. Reson.*, 1976, **24**, 71-85.

14 W. E. Kwok and Z. You, *Magn. Reson. Imaging*, 2006, **24**, 819-823.

15 E. W. McFarland and A. Mortara, *Magn. Reson. Imaging*, 1992, **10**, 279-288.

16 D. Ratering, C. Baltes, J. Nordmeyer-Massner, D. Marek and M. Rudin, *Magn. Reson. Med.*, 2008, **59**, 1440-1447.

17 A. C. Wright, H. K. Song and F. W. Wehrli, *Magn. Reson. Med.*, 2000, **43**, 163-169.

18 R. D. Black, P. B. Roemer and O. M. Mueller, *IEEE Trans. Biomed. Eng.*, 1994, **41**, 195-197.

19 R. D. Black, T. A. Early, P. B. Roemer, O. M. Mueller, A. Mogro-Campero, L. G. Turner and G. A. Johnson, *Science*, 1993, **259**, 793-795.

20 J.-C. Ginefri, L. Darrasse and P. Crozat, *Magn. Reson. Med.*, 2001, **45**, 376-382.

21 O. Girard, J.-C. Ginefri, M. Poirier-Quinot and L. Darrasse, *Rev. Sci. Instrum.*, 2007, **78**, 124703.

22 M. Poirier-Quinot, J.-C. Ginefri, O. Girard, P. Robert and L. Darrasse, *Magn. Reson. Med.*, 2008, **60**, 917-927.

23 J. G. van Heteren, T. W. James and L. C. Bourne, *Magn. Reson. Med.*, 1994, **32**, 396-400.

24 L. Darrasse and J.-C. Ginefri, *Biochimie*, 2003, **85**, 915-937.

25 M. P. McDougall and S. M. Wright, *Magn. Reson. Med.*, 2005, **54**, 386-392.

26 S. M. Wright and M. P. McDougall, *Proceedings of the 12th Annual Meeting of the International Society for Magnetic Resonance in Medicine*, Kyoto, Japan, 2004, p. 533.

27 S. M. Wright, M. P. McDougall and D. G. Brown, *Proceedings of the 11th Annual Meeting of the International Society for Magnetic Resonance in Medicine*, Toronto, Canada, 2003, p. 23.

28 S. M. Wright and M. P. McDougall, *NMR Biomed.*, 2009, **22**, 982-993.

29 M. P. McDougall, Ph.D. Dissertation, Texas A&M University, College Station, TX, 2004.

30 S. M. Wright, M. P. McDougall and D. G. Brown, *Proceedings of the 2nd Joint Conference of the Engineering in Medicine and Biology Society and the Biomedical Engineering Society*, Houston, TX, 2002, vol. 2, pp. 1181-1182.

31 J. S. Hyde, W. Froncisz, A. Jesmanowicz and J. B. Kneeland, *Med. Phys.*, 1986, **13**, 1-7.

32 A. G. Webb, *Prog. Nucl. Magn. Reson. Spectrosc.*, 1997, **31**, 1-42.

33 T. L. Peck, R. L. Magin and P. C. Lauterbur, *J. Magn. Reson., Ser. B*, 1995, **108**, 114-124.

34 Z.-H. Cho, C. B. Ahn, S. C. Juh, H. K. Lee, R. E. Jacobs, S. Lee, J. H. Yi and J. M. Jo, *Med. Phys.*, 1988, **15**, 815-824.

35 E. Odeblad, *Acta Obstet. Gynecol. Scand.*, 1966, **45**, Suppl. 2, 1-188.

36 R. W. Wiseman, T. S. Moerland and M. J. Kushmerick, *NMR Biomed.*, 1993, **6**, 153-156.

37 S. C. Grant, S. J. Blackband, A. G. Webb, G. Friedman and R. L. Magin, *Proceedings of the 1st Annual International IEEE Engineering in Medicine and Biology Society Special Topic Conference on Microtechnologies in Medicine and Biology*, Lyon, France, 2000, pp. 101-105.

38 D. L. Olson, T. L. Peck, A. G. Webb, R. L. Magin and J. V. Sweedler, *Science*, 1995, **270**, 1967-1970.

39 J. D. Trumbull, I. K. Glasgow, D. J. Beebe and R. L. Magin, *IEEE Trans. Biomed. Eng.*, 2000, **47**, 3-7.

40 S. S. Mohan, M. Hershenson, S. P. Boyd and T. H. Lee, *IEEE J. Solid-State Circuits*, 1999, **34**, 1419-1424.

41 H. M. Greenhouse, *IEEE Trans. Parts, Hybrids, Packag.*, 1974, **10**, 101-109.

42 J. N. Burghartz, D. C. Edelstein, M. Soyuer, H. A. Ainspan and K. A. Jenkins, *IEEE J. Solid-State Circuits*, 1998, **33**, 2028-2034.

43 R. P. Ribas, J. Lescot, J.-L. Leclercq, J. M. Karam and F. Ndagijimana, *IEEE Trans. Microwave Theory Tech.*, 2000, **48**, 1326-1335.

44 E. Harel, *Lab Chip*, 2009, **9**, 17-23.

45 C. Massin, G. Boero, F. Vincent, J. Abenhaim, P.-A. Besse and R. S. Popovic, *Sens. Actuators, A*, 2002, **97-98**, 280-288.

46 C. Massin, G. Boero, P. A. Eichenberger, P.-A. Besse and R. S. Popovic, *Proceedings of the 11th International Conference on Solid-State Sensors and Actuators*, Munich, Germany, 2001, pp. 784-787.

47 C. Massin, F. Vincent, A. Homsy, K. Ehrmann, G. Boero, P.-A. Besse, A. Daridon, E. Verpoorte, N. F. de Rooij and R. S. Popovic, *J. Magn. Reson.*, 2003, **164**, 242-255.

48 J. H. Walton, J. S. de Ropp, M. V. Shutov, A. G. Goloshevsky, M. J. McCarthy, R. L. Smith and S. D. Collins, *Anal. Chem.*, 2003, **75**, 5030-5036.

49 H. Wensink, D. C. Hermes and A. van den Berg, *Proceedings of the 17th IEEE International Conference on Microelectromechanical Systems*, Maastricht, The Netherlands, 2004, pp. 407-410.

50 H. Wensink, F. Benito-Lopez, D. C. Hermes, W. Verboom, H. J. G. E. Gardeniers, D. N. Reinhoudt and A. van den Berg, *Lab Chip*, 2005, **5**, 280-284.

51 K. Ehrmann, M. Gersbach, P. Pascoal, F. Vincent, C. Massin, D. Stamou, P.-A. Besse, H. Vogel and R. S. Popovic, *J. Magn. Reson.*, 2006, **178**, 96-105.

52 T. L. Peck, R. L. Magin, J. Kruse and M. Feng, *IEEE Trans. Biomed. Eng.*, 1994, **41**, 706-709.

53 S. Eroglu, B. Gimi, B. B. Roman, G. Friedman and R. L. Magin, *Concepts Magn. Reson. B*, 2003, **17**, 1-10.

54 J. S. Boyer, M.S. Thesis, Texas A&M University, College Station, TX, 1995.

55 B. Gimi, S. Eroglu, L. Leoni, T. A. Desai, R. L. Magin and B. B. Roman, *Concepts Magn. Reson. B*, 2003, **18**, 1-8.

56 J. E. Stocker, T. L. Peck, S. J. Franke, J. Kruse, M. Feng and R. L. Magin, *Proceedings of the 17th Annual Conference of the IEEE Engineering in Medicine and Biology Society*, Montreal, Canada, 1995, vol. 1, pp. 843-844.

57 C. Massin, C. Azevedo, N. Beckmann, P.-A. Besse and R. S. Popovic, *Proceedings of the 2nd Annual International IEEE Engineering in Medicine and Biology Society Special Topic Conference on Microtechnologies in Medicine and Biology*, Madison, WI, 2002, pp. 199-204.

58 M. Weiger, D. Schmidig, S. Denoth, C. Massin, F. Vincent, M. Schenkel and M. Fey, *Concepts Magn. Reson. B*, 2008, **33**, 84-93.

59 E. Wu, C.-W. Hsieh, C.-W. Liu and J.-H. Chen, *Proceedings of the 27th Annual International Conference of the IEEE Engineering in Medicine and Biology Society*, Shanghai, China, 2005, pp. 1363-1366.

60 S. Eroglu, G. Friedman and R. L. Magin, *IEEE Trans. Magn.*, 2001, **37**, 2787-2789.

61 S. M. Wright, R. L. Magin and J. R. Kelton, *Magn. Reson. Med.*, 1991, **17**, 252-268.

62 W. Froncisz, A. Jesmanowicz and J. S. Hyde, *J. Magn. Reson.*, 1986, **66**, 135-143.

63 D. I. Hoult, C.-N. Chen and V. J. Sank, *Magn. Reson. Med.*, 1984, **1**, 339-353.

64 M. Decorps, P. Blondet, H. Reutenauer, J. P. Albrand and C. Remy, *J. Magn. Reson.*, 1985, **65**, 100-109.

65 M. D. Hollett, G. P. Cofer and G. A. Johnson, *Invest. Radiol.*, 1987, **22**, 965-968.

66 M. D. Schnall, C. Barlow, V. H. Subramanian and J. S. Leigh, Jr., *J. Magn. Reson.*, 1986, **68**, 161-167.

67 S. M. Wright, *Proceedings of the 8th Annual Meeting of the Society of Magnetic Resonance in Medicine*, Amsterdam, The Netherlands, 1989, p. 955.

68 M. Utz and R. Monazami, *J. Magn. Reson.*, 2009, **198**, 132-136.

69 J.-F. Jacquinot and D. Sakellariou, *Concepts Magn. Reson. A*, 2011, **38**, 33-51.

70 D. Sakellariou, G. Le Goff and J.-F. Jacquinot, *Nature*, 2007, **447**, 694-697.

71 H. Ryan, K. Lamson, J. Elliott, A. Zaß, K. Wang, J. Korvink and M. Utz, *Proceedings of the 52nd Experimental NMR Conference*, Pacific Grove, CA, 2011, p. 167.

72 M. Utz and K. Wang, *Proceedings of the 13th International Conference on Miniaturized Systems for Chemistry and Life Sciences*, Jeju, Korea, 2009, pp. 1656-1658.

73 A. Zaß, K. Wang, J. Korvink, M. Reed, J. Landers and M. Utz, *Proceedings of the 14th International Conference on Miniaturized Systems for Chemistry and Life Sciences*, Groningen, The Netherlands, 2010, pp. 1922-1924.

74 A. Zaß, K. Wang and M. Utz, *Proceedings of the Joint Annual Meeting of the International Society of Magnetic Resonance in Medicine and the European Society for Magnetic Resonance in Medicine and Biology*, Stockholm, Sweden, 2010, p. 423.

75 T. Lanz, *Proceedings of the 16th Annual Meeting of the International Society for Magnetic Resonance in Medicine*, Toronto, Canada, 2008.

76 R. E. Collin, *Foundations for Microwave Engineering*, ed. D. G. Dudley, John Wiley & Sons, Inc., Hoboken, NJ, 2nd edn., 2001, ch. 5.5, pp. 319-330.

77 M. P. McDougall, S. M. Wright and D. G. Brown, *Proceedings of the 11th Annual Meeting of the International Society for Magnetic Resonance in Medicine*, Toronto, Canada, 2003, p. 472.

78 S. M. Wright, D. G. Brown and M. P. McDougall, *Magnetic Resonance Imaging Using a Reduced Number of Echo Acquisitions*, *US Pat.,* 6771071, 2004, http://patent.ipexl.com/US/6771071.html.

79 C. Koo, K. Feng, J. Park, M. P. McDougall, S. M. Wright and A. Han, *Proceedings of the 23rd IEEE International Conference on Microelectromechanical Systems*, Hong Kong, China, 2010, pp. 1011-1014.

80 C. Koo, R. F. Godley, J. Park, M. P. McDougall, S. M. Wright and A. Han, *Lab Chip*, 2011, DOI: 10.1039/C1LC20056A.

81 R. S. Kane, S. Takayama, E. Ostuni, D. E. Ingber and G. M. Whitesides, *Biomaterials*, 1999, **20**, 2363-2376.

82 H. Nyquist, *Phys. Rev.*, 1928, **32**, 110-113.

83 R. A. Matula, *CRC Handbook of Chemistry and Physics*, ed. W. M. Haynes, CRC Press/Taylor and Francis, Boca Raton, FL, 91st edn., 2011, ch. 12, pp. 39-40.

APPENDIX A

MATLAB® SCRIPT

MATLAB® script for comparing the frequency response of a matched and tuned coil to that of a parallel RLC circuit. Collin claims for them to be comparable for loaded Q greater than or equal to 10 (see subsection 2.2.5).

```
clear all;

Q = 37.72;
R = 2.0;
F0 = 200.128e6;
w0 = 2*pi*F0;

%Parallel RLC Ckt w/ 50ohm resistor

F = [180e6:.01e6:220e6];
Lp = 50/(w0*Q);
Cp = 1/(Lp*w0^2);

Zp = 1./(1i*2*pi*F*Cp + 1./(1i*2*pi*F*Lp) + 1/50);
RLp = 20*log10(abs((Zp-50)./(Zp+50)));

plot(F,RLp, 'green', 'linewidth', 3)
hold on
AXIS([180e6 220e6 -40 0])
xlabel('Frequency')
ylabel('Return Loss - dB')

%Matched Coil circuit

Lm = Q*R/w0;
XL = w0*Lm

Xtfull = (50*XL + ((50*R^2 + 50*XL^2)*(R - 50) + 2500*XL^2)^(1/2))/(R - 50);
Ct = -1/(w0*Xtfull);

Xmfull = (5000*R^2*XL - 100*R*XL^3 - 100*R^3*XL + ((R^4 - 50*R^3 + R^2*XL^2 +
50*R*XL^2)*(R^3 - 50*R^2 + R*XL^2 + 50*XL^2))/(2*R*XL))/(50*R*XL^2 - 50*R^3 +
R^4 + R^2*XL^2 + 2*R*XL*(50*R^3 - 2500*R^2 + 50*R*XL^2)^(1/2)) - (R^3 - 50*R^2
+ R*XL^2 + 50*XL^2)/(2*R*XL);
Cm = -1/(w0*Xmfull);

Zm = Zparallel(R + 1i*Lm*2*pi*F,1./(1i*2*pi*F*Ct)) + 1./(1i*2*pi*F*Cm);
RLm = 20*log10(abs((Zm-50)./(Zm+50)));

plot(F, RLm, 'black', 'linewidth', 1)

hold off
```

APPENDIX B

VARACTOR TESTING DATA

Data acquired with the HP 4195A network analyzer and impedance test adapter to evaluate the capacitance and equivalent series resistance (ESR) of two different varactor diodes. Resistance measurements below .1 Ω (highlighted in red) are not meaningful, due to the limits of reflection-type impedance measurements. Graphs and analysis are in subsection 3.2.3. Data matches reasonably well with the limited information available in datasheets. Datasheets:

http://www.microsemi.com/misc/lstvw/images/pdf.gif

http://de.sitestat.com/infineon/infineon/s?infineon.en.product.findProductTypeByName.html_dgdl_bb639_bb659series.pdf&ns_type=pdf&ns_url=http://www.infineon.com/dgdl/bb639_bb659series.pdf?folderId=db3a304313d846880113d98def1d0130&fileId=db3a304313d846880113d9bc2d2e015e

Accessed May 23rd, 2011.

Infineon BB639					**Microsemi MV34009**			
V_{bias}	**C_s (pF)**	**R_s (Ω)**	**Q**		**V_{bias}**	**C_s (pF)**	**R_s (Ω)**	**Q**
0	61.8	0.664	19.4		0	28.3	0.665	42.3
1	40.6	0.655	29.9		1	14.1	0.743	76.0
2	31.2	0.647	39.4		2	8.45	0.758	124.2
3	25.3	0.640	49.1		3	5.77	0.625	220.7
5	17.6	0.626	72.2		4	4.32	0.496	371.4
7	12.6	0.607	104.0		5	3.42	0.376	618.8
10	8.24	0.558	173.1		7	2.4	0.192	1726.9
15	4.86	0.430	380.8		9	1.83	*0.052*	*8362.5*
20	3.5	0.308	738.2		12	1.5	*-0.028*	*-18947.0*
25	2.87	0.237	1169.9		15	1.47	*-0.035*	*-15467.0*
30	2.55	0.213	1465.1					
35	2.43	0.217	1509.1					
40	2.38	0.233	1435.0					

VITA

Name: Richard Franklin Godley

Address: Dept. of Electrical Engineering
Texas A&M University
College Station, TX 77843-3128

Email Address: rgodley@gmail.com

Education: B.S., Engineering, Electrical Concentration, LeTourneau University, 2009

M.S., Electrical Engineering, Texas A&M University, 2011